Nuclear Engineering Education Research (NEER)
Final Scientific/Technical Report

Mechanism of Irradiation Assisted Cracking of Core Components in Light Water Reactors

Grant #DE-FG07-99ID13768
Project No. 99-1637

Submitted by:
University of Michigan
Gary S. Was, PI
Michael Atzmon, co-PI
Lumin Wang, co-PI
Jeremy Busby

Submitted on:

April 30, 2003

Executive Summary

The overall goal of the project is to determine the mechanism of irradiation assisted stress corrosion cracking (IASCC). IASCC has been linked to hardening, microstructural and microchemical changes during irradiation. Unfortunately, all of these changes occur simultaneously and at similar rates during irradiation, making attribution of IASCC to any one of these features nearly impossible to determine. The strategy set forth in this project is to develop means to separate microstructural from microchemical changes to evaluate each separately for their effect on IASCC. In the first part, post irradiation annealing (PIA) treatments are used to anneal the irradiated microstructure, leaving only radiation induced segregation (RIS) for evaluation for its contribution to IASCC. The second part of the strategy is to use low temperature irradiation to produce a radiation damage dislocation loop microstructure without radiation induced segregation in order to evaluate the effect of the dislocation microstructure alone.

A radiation annealing model was developed based on the elimination of dislocation loops by vacancy absorption. Results showed that there were indeed, time-temperature annealing combinations that leave the radiation induced segregation profile largely unaltered while the dislocation microstructure is significantly reduced. Proton irradiation of 304 stainless steel irradiated with 3.2 MeV protons to 1.0 or 2.5 dpa resulted in grain boundary depletion of chromium and enrichment of nickel and a radiation damaged microstructure. Post irradiation annealing at temperatures of 500 – 600°C for times of up to 45 min. removed the dislocation microstructure to a greater degree with increasing temperatures, or times at temperature, while leaving the radiation induced segregation profile relatively unaltered. Constant extension rate tensile (CERT) experiments in 288°C water containing 2 ppm O_2 and with a conductivity of 0.2 μS/cm and at a strain rate of 3×10^{-7} s^{-1} showed that the IASCC susceptibility, as measured by the crack length per unit strain, decreased with very short anneals and was almost completely removed by an anneal at 500°C for 45 min. This annealing treatment removed about 15% of the dislocation microstructure and the irradiation hardening, but did not affect the grain boundary chromium depletion or nickel segregation, nor did it affect the grain boundary content of other minor impurities. These results indicate that RIS is not the sole controlling feature of IASCC in irradiated stainless steels in normal water chemistry.

The isolation of the irradiated microstructure was approached using low temperature irradiation or combinations of low and high temperature irradiations to achieve a stable, irradiated microstructure without RIS. Experiments were successful in achieving a high degree of irradiation hardening without any evidence of RIS of either major or minor elements. The low temperature irradiations to doses up to 0.3 dpa at T<75°C were also very successful in producing hardening to levels considerably above that for irradiations conducted under nominal conditions of 1 dpa at 360°C. However, the microstructure consisted of an extremely fine dispersion of defect clusters of sizes that are not resolvable by either transmission electron microscopy (TEM) or small angle x-ray scattering (SAXS). The microstructure was not stable at the 288°C IASCC test temperature and resulted in rapid reduction of hardening and presumably, annealing of the defect clusters at this temperature as well. Nevertheless, the annealing studies showed that treatments that resulted in significant decreases in the hardening produced small changes in the dislocation microstructure that were confined to the elimination of the finest of loops (~1 nm). These results substantiate the importance of the very fine defect microstructure in the IASCC process.

The results of this program provide the first definitive evidence that RIS is not the sole controlling factor in the irradiation assisted stress corrosion cracking of austenitic stainless steels in normal water chemistry. Earlier research has suggested that RIS may not play the dominant role it has recently been afforded, but the results of this program are the first to definitively establish this role. The program has also shown that the fine defect structure is implicated in the IASCC process and likely plays a role in the observed cracking of core components. The results of this project provide the basis and the motivation for further investigation into the mechanism of IASCC in which fine defect clusters may play a crucial, if not a defining role.

TABLE OF CONTENTS

List of Tables

List of Figures

288°C, 0.2 μS/cm, and 2 ppm O_2. A line has been added to the fracture surface of the sample annealed at 500°C for 45 min. to indicate the irradiated surface of the sample.

Figure 15: Comparison of annealing behavior of major alloying elements, a.), minor alloying elements, b.), dislocation loop line length, c.) and hardness, d.) with cracking susceptibility for CP-304 irradiated to 1.0 and 2.5 dpa.

Figure 16: Schematic of annealing behavior of mixed population of black-dot damage and dislocations. During annealing, small defect clusters are removed or dissociate into individual interstitials which may then be absorbed by dislocation loops. This process results in a population of larger loops with no change in density.

Figure 17: Comparison of measured and simulated annealing of small dislocation loop populations from proton irradiations to 1.0 dpa at 360°C (plotted as Nd in c.)).

Figure 18: Comparison of slip bands in CP 304 SS irradiated to 1.0 dpa at 360°C and annealed at a.) 450°C/45 minutes (IG with 65 slip band systems/mm^2) or b.) 500°C/45 minutes (no IG and 25 slip band systems/mm^2). Also shown in c.) are the slip bands observed on a CP 304 SS sample irradiated to 0.3 dpa at 360°C (no IG with 22 slip band systems/mm^2) and d.) 0.3 dpa at < 75°C (no IG with 28 slip band systems/mm^2). Samples strained at 3.5 x 10^{-7} s^{-1} in water at 288°C, 0.2 μS/cm, and 2 ppm O_2.

Figure 19. Change in hardness of CP304 SS following annealing of samples irradiated to 0.3 dpa at T<75°C.

Figure 20. Composition profiles for Cr, Ni, Fe and Si across grain boundaries of CP304 SS following low temperature irradiation at T<75°C showing the lack of RIS.

Figure 21. Scheme for achieving a stable irradiated microstructure by combining high temperature (T=360°C) and low temperature (T<75°C) irradiation in increments of 0.25 dpa.

Figure 22. Stress-strain curves of CP304SS samples tested in normal water chemistry consisting of 288°C water containing 2 ppm O_2 and conductivity of 0.2 μS/cm. Samples were irradiated to the following conditions: a) 0.25 dpa @ T<75°C + 0.25 dpa @ 360°C, b) 0.25 dpa @ 360°C + 0.25 dpa @ 360°C, c) 0.25 dpa @ 360°C + 0.25 dpa @ T<75°C, and d) 0.25 dpa @ 360°C + 0.25 dpa @ T<75°C + 0.25 dpa @ 360°C.

Figure 23. Change in hardness of CP304SS following irradiation to 0.3 dpa and annealing at 288°C for various times up to 24 hours.

Figure 24: Comparison of annealing of samples irradiated at low temperatures with model simulations of annealing of small defect clusters.

Figure 25: Comparison of annealing of samples irradiated at low temperatures with predictions from model developed by Simonen.

1.0 INTRODUTION

Irradiation assisted stress corrosion cracking (IASCC) describes the intergranular cracking that occurs in irradiated structural components in water reactors. The general feature common to these failures is increased susceptibility of various non-sensitized austenitic stainless steels (SS) with neutron fluence. Incidents of IASCC were first reported in the early 1960's [1] in 304, 304L and 347 SS fuel rod cladding in BWRs, [2-4] and more recently in 304 SS fuel cladding in the Connecticut Yankee reactor (PWR). [5] IASCC also occurs in 304 SS control rod absorber tubes, fuel bundle cap screws, control rod blade handles, sheaths and follower rivets, plate type control blades and instrument dry tubes in BWRs. Brown and Gordon [6,7] reported detailed IASCC field histories in BWRs, including cracking in Alloy 600 shroud head bolts (first observed in 1986), stainless steel safe ends (1984) and in-core instrumentation tubes (1984). At the West Milton PWR test loop, intergranular failure of vacuum annealed type 304 stainless steel fuel cladding was observed [8] in 316°C ammoniated water (pH 10) when the cladding was stressed above yield. Similarly, IASCC was observed in creviced stainless steel fuel element ferrules in the Winfrith SGHWR, [9] a 100 MWe plant in which light water is boiled within pressure tubes.

IASCC occurs irrespective of reactor type. Specific BWR vs. PWR comparisons were performed using in-core swelling tubes [1,10] fabricated from a variety of commercial and high purity heats of types 304, 316 and 348 stainless steel and Alloys X-750, 718 and 625. Based on identical strings of specimens placed in fuel rod locations, there was little distinction in the IASCC response between the two reactor types. [11] Thus, it is becoming increasingly evident that the problem is widespread without regard to environment or alloy, and that numerous core components may be susceptible to this form of degradation. A recent review by Andresen [1] identified failures in some 17 components, spanning 6 iron- or nickel-base alloys and 4 reactor designs. Given that a threshold in fluence has been identified, many of the susceptible components may just now be coming to our attention and the extent of the problem may continue to expand.

The future of current light water reactors and future water reactor concepts may well rest on the solution to the IASCC problem. It is clear that stress, an irradiated microstructure and an

aggressive environment are all required for IASCC to occur. Further, the microstructural features due to irradiation are generally well known. What is not known is which of these features is responsible for IASCC and why. This program seeks to answer the first part of this question; what microstructural features are responsible for IASCC. The following section provides background on the IASCC phenomena along with the specific objective of this program and the approach to the problem.

2.0 BACKGROUND

2.1 Possible Mechanisms of IASCC

Since irradiation by high energy neutrons can affect both the material properties and the environmental chemistry, IASCC is a complex problem which is neither easy to investigate practically nor simple to understand mechanistically. [10] The mechanisms which have been proposed to explain IASCC are categorized into either effects of radiation on the "environment", such as corrosion potential and ion chemistry, or "persistent" effects on the microstructure such as radiation hardening and creep, and on the microchemistry such as radiation-induced segregation of alloying elements and impurities. While the environment can affect the degree of cracking, it is the "persistent" effect of irradiation on the material that is primarily responsible for its susceptibility. This point is supported by the observation of a distinct threshold fluence (1 dpa in BWRs and 3-5 dpa in PWRs) at which IASCC occurs. [10] The existence of a threshold fluence for IASCC both in-situ and in post-irradiation tests indicates that "persistent" radiation effects (microstructural and microchemical changes) are crucial for IASCC. This position was emphasized by a jointly sponsored (DOE & EPRI) Radiation Assistance Task Force on radiation materials science at a workshop held in March, 1998. [12] Thus, the key to understanding the mechanism is understanding the radiation effect on the material. This amounts to two possible irradiation-induced changes; those that alter the microstructure and those, which alter the microchemistry.

Microstructure effects are predominantly faulted dislocation loops and an increase in the dislocation network density. Radiation induced precipitation (phase changes) and bubble formation do not occur at typical LWR temperatures and doses and voids are rarely observed.

The dislocation loops range from small, unresolvable "black dots" to larger Frank-type faulted loops between 8 and 12 nm in diameter. From the standpoint of cracking, their significance is twofold; they result in lattice hardening by acting as hard barriers to dislocation motion, and they cause strain localization (dislocation channeling), in which plastic deformation occurs inhomogeneously in groups of slip bands through which a lead dislocation has passed and removed the obstacles for subsequent dislocation motion. While it is unknown how such localization of strain relates to IG cracking, it remains a strong possibility that there is a relation between the deformation mode and cracking. However, experiments conducted to date are inconclusive due to the fact that strain localization and the causative microstructure always occur simultaneously with a change in microchemistry at the grain boundaries.

Local composition changes occur as a result of radiation induced segregation (RIS) of both major alloying elements and impurities. In austenitic alloys, these changes can be quite substantial with the contents of majority elements (Cr, Ni) changing by a factor of 2 or more and impurities enriching by factors approaching 100. There is strong suspicion that such significant composition changes at the grain boundary are responsible for the observed IASCC. In fact, a very likely mechanism for IASCC observed both in-plant and in the laboratory is chromium depletion due to RIS. The loss of a protective chromium film due to depletion of chromium at the grain boundaries resulting from chromium carbide precipitation during heat treating was the cause of the BWR pipe cracking problem in the 70s and 80s. [13] In fact, high temperature, oxidizing environments have been shown repeatedly to produce intergranular stress corrosion cracking in chromium depleted austenitic iron- and nickel-base alloys. [14] Although the chromium-depleted zones caused by RIS are much narrower (by 100x) than those produced by carbide precipitation, they have also been associated with IGSCC in oxidizing media, such as exist in a BWR. However, the problem is that IASCC also occurs in PWRs, which have reducing environments that are known to be benign to chromium depletion. Herein lies the major problem: while cracking morphology and dose dependence are nearly identical in oxidizing (BWR) and reducing (PWR) systems (except for a higher dose threshold in PWRs), chromium depletion can explain cracking in the former but not in the latter. Further, it is

unlikely that impurity segregation is the determining factor since cracking susceptibility is no different for high-purity heats both in-plant and in the laboratory. [15]

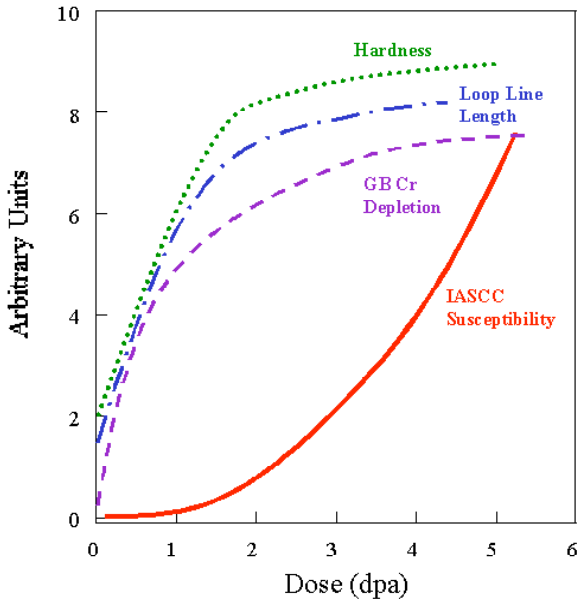

Figure 1. Schematic of the development of dislocation loop microstructure, hardening and RIS along with the increase in IASCC with irradiation dose.

Significant amounts of cracking data can be shown to correlate to both the development of the dislocation microstructure and radiation induced segregation. Figure 1 schematically depicts the problem in attributing IASCC to a particular irradiation induced microstructural change. As the figure shows, cracking increases with dose, but so does the dislocation microstructure, hardening (which results from the microstructure) and the degree of radiation induced segregation. Hence, while it has been shown that changes to the material control IASCC, it remains unclear whether microstructure changes or microchemistry changes or some combination of the two are controlling. This point was underscored by the Cooperative IASCC Research Program (CIR), an international group of reactor vendors, utilities and regulators, which identified the uncertainty of the relative roles of microstructure and microchemistry as the principal barrier to solving the IASCC problem. It is possible that some other factor may be controlling cracking. However, the search for an unknown is pointless until it can be shown that neither microstructure nor microchemistry control IASCC. The solution to the IASCC problem

must begin with an understanding how each of these principal irradiation-induced changes affect cracking in oxidizing and reducing environments, as stated in the following objective.

2.2 Objective

The objective of this program is to determine the mechanism of IASCC of core components in austenitic light-water reactor core components. The premise is that IASCC is caused either by radiation induced segregation (RIS) at the grain boundary, or by the radiation induced dislocation microstructure. This program will week to identify the causative factors of IASCC by first isolating, and then independently evaluating the roles of microstructure and microchemistry in SCC susceptibility.

2.3 Approach

We will identify the "persistent" effect responsible for IASCC by separating the microstructure changes from the microchemistry changes. That is, we will create a microstructure typical of that resulting from neutron irradiation in reactor to several dpa, but with *little change* in microchemistry from the unirradiated state. Similarly, we will create a microchemistry typical of that resulting from neutron irradiation in-reactor to several dpa, but with *little change* in microstructure from the unirradiated state. In this way, we can perform SCC tests to isolate the key material condition that is responsible for the observed cracking. We do not expect to completely eliminate one feature while completely retaining the other, but we do expect that the feature of interest will strongly dominate the other. We will then be able to conduct more specific investigations into the mechanism by which microstructure or microchemistry changes affect the IG cracking process.

We propose to create these microstructures using proton irradiation. This has developed, over the past 10 years, into a proven technique for producing representative microstructures in both 304 and 316 SS and in high purity analogues without significant residual radioactivity, at a much lower cost and without the large amounts of time and expense required to conduct in-reactor irradiations. In fact, this is the only practical way to conduct a mechanistic study of the

problem of IASCC.

The end result of this program will be the identification of the material changes that affect IASCC and a better understanding of the mechanism. Until such changes are identified, no further progress can be made on identifying the mechanism and solving the problem. Solving the IASCC problem is a long-term goal, but not the objective of this proposal. An understanding of the mechanism will allow for the development of mitigation strategies for existing core components and also the development of radiation-resistant alloys or microstructures for replacement components and for advanced reactor designs. These developments are essential to the extension of existing plants to longer lives and the prevention of IASCC in advanced reactor designs. This strategy has the support of EPRI as evidenced by the substantial cost sharing provided in the budget.

2.4 The Research Plan

The plan diagrammed in Fig. 2 is based on isolating the relevant LWR microstructure and microchemistry. Experiments will be conducted on a high purity Fe-Cr-Ni-Mn alloy (304 SS analogue) and selected experiments will be conducted on archive samples of a commercial 304 SS alloy. The high purity alloy (selected to avoid complications from impurities) will be cold-worked and annealed to produce a grain size of 10-12 micrometers. The commercial alloy was irradiated in reactor and was shown to be susceptible to IASCC via constant extension rate tensile tests. [15] An extensive characterization of its microstructure and microchemistry has been conducted by PNNL and we have shown that both can be replicated by proton irradiation. [17-21] Hence, this alloy represents the ideal case for studying microstructure and microchemistry effects using proton irradiation. Irradiation will be conducted using 3.2 MeV protons generated in the Tandetron accelerator at the Michigan Ion Beam Laboratory at the University of Michigan. This produces a nearly flat damage profile over the first 35 μm, followed by a damage peak at ~40 μm. [22] Characterization of microstructure and microchemistry changes will be made in the flat damage region, away from the surface and the damage peak. Microstructure characterization will be made in TEM and microchemistry characterization will be made using STEM-EDS.

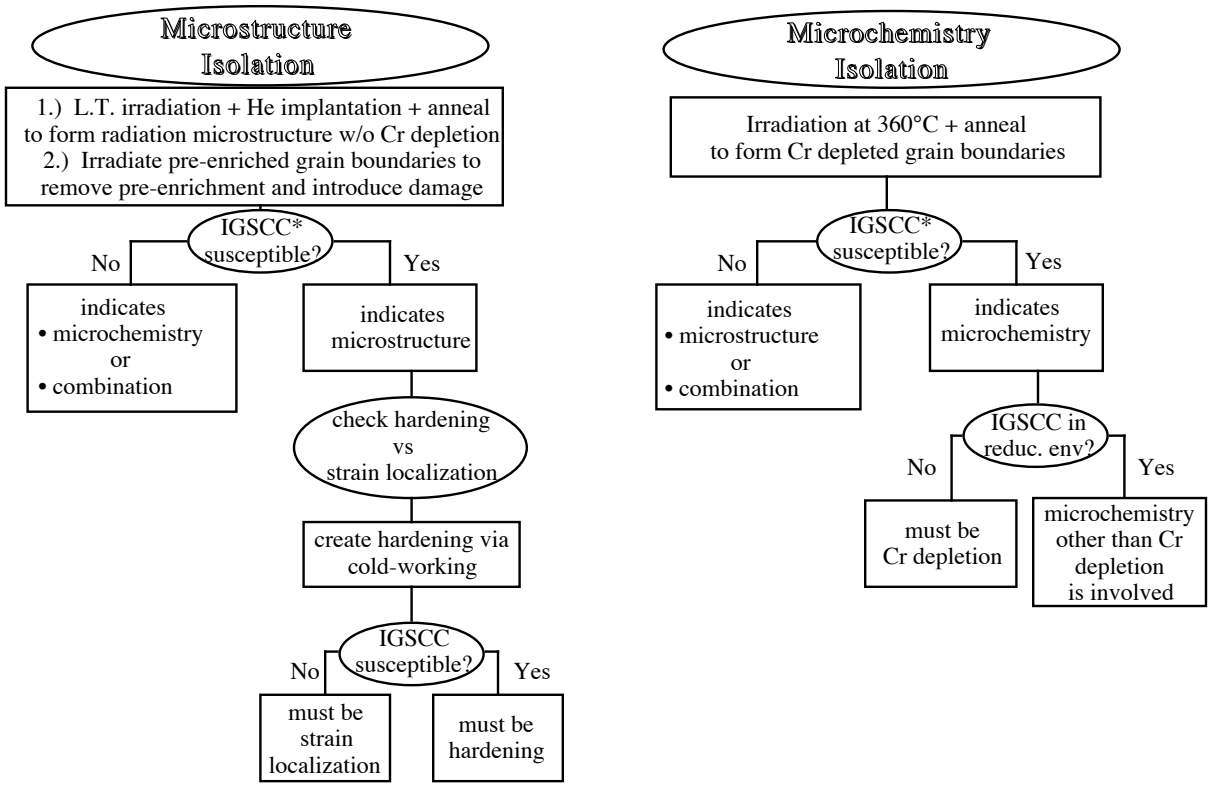

*IASCC experiments are conducted in oxidizing environments (288°C, pH 7.0, O_2~2 ppm, E_{corr} ~ +150 mV_{SHE}, flowing system) and at a constant extension rate of 1 x 10^{-7} s^{-1}.

14

Figure 2. Experimental plan for isolating microstructure and microchemistry in irradiated 304SS.

IASCC experiments will be conducted in a specially designed flowing autoclave system in which water chemistry (corrosion potential, oxygen content, solution conductivity, pH, flow rate), temperature, pressure and strain rate can be controlled on four samples tested independently. [23] Cracking susceptibility is evaluated by the number and length of cracks in the irradiated region of the sample over the course of a constant extension rate test. (Note that because the irradiated layer is 40 μm deep and the bulk is ductile, the sample will not readily fail upon formation of the first crack.) We will also conduct a limited number of interrupted tests to determine crack nucleation time and an estimate of the crack growth rate. [24,25]

It is important to note that this program involves multiple experimental and analysis capabilities, each of which may constitute a project in itself. We are in a position to bring all of these techniques to bear on this problem in a single proposal because of the extensive effort that has been conducted over the past 10 years to develop and validate this technique for studying neutron irradiation damage. Thus, the specifics of proton irradiation (including dose and

temperature control), microstructure analysis, microchemistry analysis and SCC testing in relevant BWR and PWR environments have all been established. [26] The verification of the method has also been well established. [27] This program will benefit from prior work in that the entire project can be devoted to solving the IASCC problem, rather than to developing a capability.

3.0. EXPERIMENT

3.1 Material Preparation

Two 304 alloys, a high purity, low carbon alloy made by General Electric, Schenectady, and a commercial purity 304 stainless steel alloy from ABB Atom, with the compositions listed in Table 1 (in at%) were used in this study. The UHP-304L, in the form of 12 mm thickness bars, were solution annealed at 1100°C for 1 hour to produce a homogeneous microstructure and microchemistry, and a grain size of approximately 100-200 μm. The alloys were then cold rolled from 12 mm down to 2 mm to provide a reduced grain size upon recrystallization. These bar samples were then wet-polished using 320-600 grit silicon carbide (SiC) paper to remove the mechanical damage introduced during machining. The final annealing treatment in a flowing argon atmosphere at 850 °C for 30 min recrystallized the alloys to achieve grain sizes of approximately 10 μm. The commercial alloy was used in the as-received condition and had a grain size of approximately 50 microns. The CP304 alloy was archive material from the same heat that had also been irradiated in the Bärseback 1 reactor in Sweden. [28] Microstructural, microchemical, hardness and IASCC data was measured previously as a function of dose. [29]

Table 1: Bulk composition of HP-304L and CP-304 alloy as determined by electron microprobe analysis (wt% and at%)

	Cr	Ni	Fe	Mn	Mo	Si	B	C	N	P	S
HP-304L											
wt%	19.7	9.5	69.7	1.12	0.02	0.01	--	0.006	<0.001	0.001	0.002
at%	20.9	9.0	69.0	1.1	0.01	0.02	--	0.028	<0.004	0.002	0.003
CP-304											
wt%	18.3	8.5	70.6	1.38	0.37	0.65	<0.0004	0.035	0.068	0.03	0.03
at%	19.3	7.9	69.4	1.4	0.21	1.27	<0.002	0.16	0.266	0.06	0.050

3.2 Proton Irradiation

Samples for post-irradiation annealing studies were irradiated with 3.2 MeV protons to doses 1.0 or 2.5 dpa at a dose rate of approximately 4×10^{-6} dpa/s, resulting in a nearly uniform damage rate throughout the first 35 μm of the proton range (40 μm), Fig. 3. The sample temperature during irradiation was maintained at 360° ± 10°C. A displacement energy of 25 eV

was used for dose calculations throughout this paper. Further details of the sample preparation and irradiation are given elsewhere. [30] Following irradiation, samples were annealed in a small tube furnace in a flowing Ar gas stream at temperatures ranging from 400ºC to 650ºC for times of 45 or 90 minutes and then quenched in water.

Low temperature irradiations for microstructure analysis were conducted to doses of 0.25 to 1.5 dpa dpa with 3.2 MeV protons at a temperature of no greater than 75°C. A reduction in dose rate to 5 □ 10^{-7} dpa/s was required to maintain the low sample temperature, which was monitored with three J-type thermocouples and was kept at less than 75°C throughout the irradiation. Following low temperature irradiation, samples were annealed in a vacuum furnace at 350°C for either 8 minutes or 15 minutes.

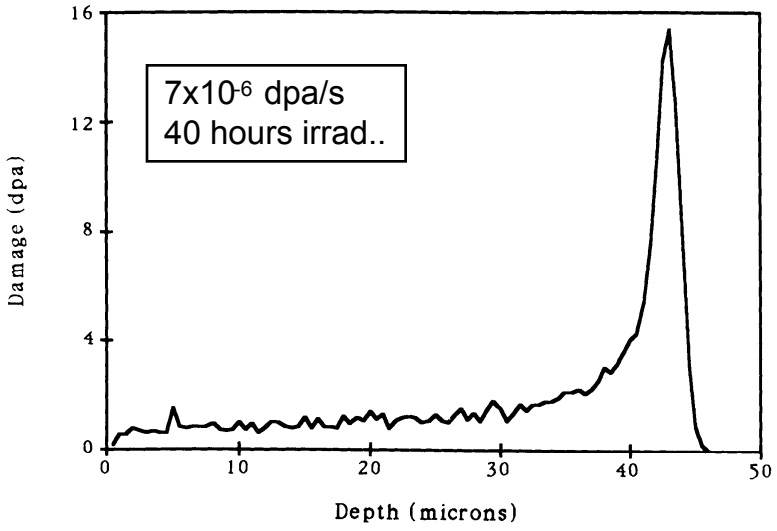

Figure 3. Displacement rate profile for 3.2 MeV protons in stainless steel as calculated by the Monte Carlo program TRIM 90.

3.3 Radiation Induced Segregation

Microchemical analysis was performed before and after annealing using a scanning transmission electron microscope with energy-dispersive x-ray analysis (STEM/EDS). The STEM/EDS analysis was performed in a Philips CM200/FEG at Oak Ridge National Laboratory, which produces a probe approximately 1.2 nm in diameter (full-width, half-maximum) while operating at 200kV. STEM/EDS measurements were performed on “edge-on” grain boundaries

so as to minimize broadening of the boundary profile. Details of the grain boundary measurement technique are given in ref. [31].

3.4 Microstructure Analysis

The dislocation microstructures of samples irradiated at 75°C and 360°C, both before and after annealing were analyzed using JEOL 2010F/FEG and JEOL 4000 instruments at the North Campus Electron Microscopy Analysis Laboratory at the University of Michigan and the CM200/FEG at ORNL. For bright-field imaging (BF), a two-beam condition at **g**=[200] (close to the <110> zone axis) was used. The dark-field, rel-rod technique was also utilized. Most dislocation loop images were taken at magnifications of 100-200kx.

3.5 Post-irradiation Hardness Measurement

Hardening for the proton-irradiated alloys was measured using a Vickers hardness indenter (MICROMET II) with a load of 25 g. This load was used to confine the plastic zone ahead of the indenter tip to a depth within the proton range (~40 μm) to ensure that unirradiated material is not being sampled. The yield strength of the proton-irradiated heats is a useful parameter for comparison to existing literature data on changes in yield strength. While yield strength cannot be determined directly from the proton-irradiated samples, correlations have been developed which allow calculation of expected yield strength from dislocation microstructure or hardness. The yield strength change associated with irradiation can be estimated using

$$\Delta\sigma_y = 3.55\,\Delta H_v \quad \text{for doses} < 2.0 \text{ dpa} \qquad (1)$$
$$\Delta\sigma_y = 2.69\,\Delta H_v \quad \text{for doses} > 2.0 \text{ dpa}$$

where $\Delta\sigma_y$ is expressed in MPa and $\Delta\sigma_v$ is expressed in kg/mm^2. [32]

3.6 Stress Corrosion Cracking Experiments

The constant extension rate tensile (CERT) tests were conducted in a multiple-specimen CERT test system, supplied by Korros Data. The Korros Data system is capable of straining four samples in parallel, thus providing identical conditions within a given test. Samples were strained to failure at a rate of 3×10^{-7} s^{-1}. Details regarding the KorrosData system are published elsewhere [33].

CERT tests were performed in normal water chemistry (NWC) characterized by a water temperature of 288°C, water conductivity of 0.2 μS/cm and oxygen content of 2 ppm. The conductivity and oxygen composition were selected to arrive at a value of the corrosion potential of about +150 $mV_{SHE,}$ representative of BWR cores. [34] The dissolved oxygen concentration was controlled at 2 ppm by bubbling a 5% O_2/Ar mixture through the water reservoir. Conductivity was controlled via automatic additions of dilute H_2SO_4 so that the outlet conductivity was maintained at 0.2 μS/cm. The electrochemical potential was verified for the NWC environment. A Cu/CuO reference electrode with a yttria-stabilized zirconia membrane was used in conjunction with an EG&G Model 173 Potentiostat. A spare CP-304 tensile sample was used as the working electrode. For the NWC described, the measured potential was +140 mV_{SHE}.

Fractography was performed following each CERT test using a Philips XL30/FEG SEM. While qualititative fractrography is informative in determining the type of failure and general trends, it does not provide any quantititative information about the cracking. Intergranular (IG) fracture is typically characterized by measurements of the area of IG facets on the fracture surface and expressed as an area based percentage. However, since proton irradiation only affects the first 40 μm of the irradiated face, the majority of the fracture surface is unirradiated material. Therefore, the IG cracking fraction (or percentage) for these samples refers to the irradiated area (40 μm) only.

4.0 RESULTS AND DISCUSSION

The project results will focus on post-irradiation annealing to isolate RIS and on the use of low temperature irradiation to isolate the irradiated microstructure. Section 4.1 covers the simulation of post-irradiation annealing and section 4.2 covers the experimental results. Section 4.3 provides a discussion of results of simulation and experiment to isolate RIS. Section 4.4 covers the formation of an irradiated microstructure without RIS by low temperature irradiation.

4.1 Post-Irradiation Annealing: Simulation Results

During post-irradiation annealing at low to moderate temperatures (< 700°C), the removal of composition gradients will be governed by the equilibrium vacancy concentration. The irradiation-induced composition gradients at grain boundaries will drive the motion of thermal defects during annealing. The modified inverse-Kirkendall (Perks) model developed by Allen [27] was used to simulate the behavior of composition gradients during post-irradiation annealing of 304 SS alloys. The modified inverse-Kirkendall (MIK) model is capable of handling up to three major alloying elements, and thus, was used to simulate the annealing behaviors of only Cr, Fe, and Ni. For the HP-304L alloy with the nominal composition listed in Table 1, the measured segregation profile at 1.0 dpa was used as the initial condition for annealing simulations. To simulate annealing conditions, the displacement rate was simply set equal to zero. No other modifications to the model were necessary. Annealing of segregation profiles was simulated over a wide range of temperatures (350°C to 600°C) and times (up to 10^7 sec). The annealing of grain boundary Cr depletion is shown in Figure 4 as a function of time for anneals at 400°C, 500°C, and 600°C. Simulations indicate that at least 10^6 sec and ~ 1 h at 400°C and 500°C, respectively, are required to cause grain boundary depletion to be reduced to 90% of the as-irradiated condition. However, for annealing at 600°C, 10% of the as-irradiated degree of depletion is removed in only 30 seconds.

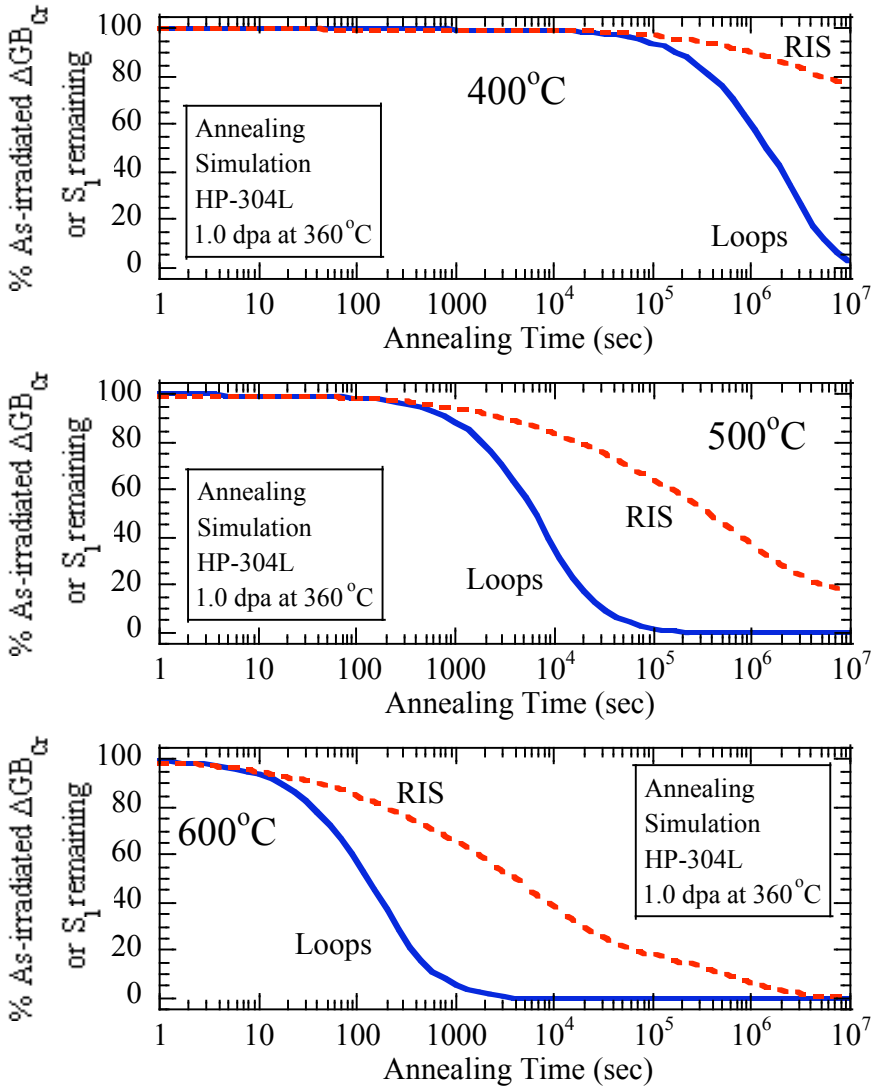

Figure 4: Comparison of simulated annealing of fraction of as-irradiated grain boundary Cr depletion and total loop line length as a function of time for anneals at 400°C, 500°C, and 600°C. Simulation for CP-304 irradiated to 1.0 dpa at 360°C.

4.1.1 Simulated annealing of dislocation loops and hardness

During post-irradiation annealing, faulted, interstitial loops will absorb thermal vacancies and shrink in size. The rate of absorption, and hence rate of change in loop size, is also affected by the line tension and stacking fault energy. In order to simulate the effects of post-irradiation annealing for a population of interstitial dislocation loops, a model was developed to calculate

the changes in loop radius and density as a function of time at any given temperature. For a population of defects widely spaced in comparison to their size, the vacancy diffusion field around each loop is assumed to be spherically symmetrical. The diffusion equation for motion of vacancies to a loop is given as:

$$\frac{d}{dr}\left(r^2 D \frac{dC}{dr}\right) = 0 \qquad (2)$$

where r is the radial distance from the dislocation loop, D is the vacancy diffusion coefficient, and C is the vacancy concentration. This equation can be solved by integration using the boundary conditions; $C = C_d$ at $r = r_d$ and $C = C_{eq}$ at $r = R$, where r_d is the loop radius, C_d is the vacancy concentration at the loop, R is a characteristic distance, and C_{eq} is the thermal equilibrium concentration of vacancies. The flux of vacancies at the loop can be written as:

$$\frac{dn}{dt} = -4\pi r_d^2 \left(\frac{dC}{dr}\right)_{r=rd} = 4\pi r_d D (C_d - C_{eq}) \qquad (3)$$

Following the methodology used by Burton [35], the rate of change of loop radius is given by:

$$\frac{dr}{dt} = -2b^2 C_{eq} D\{1 - \exp(-(U/br + \gamma/b)b^3/kT)\} \qquad (4)$$

where $U (\alpha Gb^2/2)$ is the dislocation line energy, γ is the stacking fault energy, k is the Boltzmann constant, T is the absolute temperature, G is the shear modulus, and b is the magnitude of the Burgers vector. Note that the form of Eq. (4) indicates that larger loops are removed more slowly than smaller loops. This is reasonable, as larger loops will be more stable (i.e. less excess free energy per interstitial) and more vacancies are required to annihilate the interstitials within a larger loop.

In order to simulate the annealing behavior of a population of dislocation loops, Eq. (4) was applied to every size group within a population. For a given time step, the amount of change in loop radius and the radius at the end of the time step were calculated for each group in the population. The model then iterates over time and recalculates the rate of radius change for each group. When the radius of any group shrinks below 1 nm, the group is removed from the

population, thereby reducing the dislocation loop density. While loop size distributions are informative, quantities such as total loop line length are more meaningful as they give a more complete description of the dislocation sink strength in the irradiated microstructure. Total loop line length, S_l, can be calculated as:

$$S_l = 2\pi \sum_{\text{All groups},i} r_i N_i \quad (5)$$

In a similar fashion, Nd (which is proportional to the change in yield stress according to the dispersed barrier hardening model [36]) can also be calculated.

The dislocation loop population of the HP-304L alloy irradiated with protons to 1.0 dpa at 360°C was used as the starting condition for a series of simulated anneals over a wide range of times and temperatures. The annealing of this dislocation loop population is shown as a function of time in Figure 2 for anneals at 400°C, 500°C, and 600°C. As the temperature increases from 400°C to 600°C, the time to remove 10% of the as-irradiated loop population drops from 10^5 sec to ~10 sec.

The removal of RIS and dislocation loops during post-irradiation annealing is compared directly in Figure 4. Clearly, the simulations indicate that the dislocation microstructure is removed preferentially. In order to determine the origin of the difference in the simulated removal rates, both thermodynamic and kinetic processes are considered. Specifically, the apparent activation energy is determined for the removal of both RIS and dislocation loops. Both the density of vacancies required and potential competition for thermal vacancies between RIS and dislocation loops are also considered.

4.1.2 Thermodynamic considerations

The removal of both loops and RIS reduces the excess free energy of the system. If dislocation loop formation during irradiation increases the free energy of the system more than that due to the presence of segregation profiles, the driving force for dislocation loop removal will be greater than that for RIS. Since the annealing of both RIS and dislocation loops is dependent upon the formation and diffusion of vacancies, it may be possible to gain some insight into the energetics of the removal processes. Removal of dislocation loops and RIS during post-

irradiation annealing is analogous to the removal of cold work during the recovery stage of annealing which follows a simple activation or Arrhenius type law:

$$\frac{1}{\tau} = A\, e^{(-Q/kT)} \quad . \tag{6}$$

This type of relationship was used to determine the activation energy for removing a dislocation loop population and segregation profiles. The time for removal of 90% of either, τ_{90}, was determined from simulations as a function of post-irradiation annealing temperature. Simulation of microstructure annealing was accomplished using Eq. (4) and simulation of RIS was performed using the MIK model. The natural logarithm of $1/\tau_{90}$ is plotted as a function of the inverse-temperature for the annealing of both RIS and dislocation loops in Figure 5 and the slope of the least-squares fit gives the apparent activation energy. From Figure 5, the apparent activation energies for removal of RIS and dislocation loops are 3.1 and 2.5 eV, respectively.

The removal of both dislocation loops and RIS profiles is dependent on diffusion processes. The apparent activation energy determined from Eq. (6) and Figure 5 for removal of RIS profiles is 3.1 eV. No combination of input diffusion parameters to the MIK model matches this value exactly, but the vacancy formation and migration energies for Ni are the closest (1.79 and 1.04 eV, respectively). [27] The total energy required for motion via Ni atoms is 2.83 eV. While lower than the calculated value, Ni-vacancy diffusion is a sensible mechanism since both Cr depletion and Ni enrichment profiles must be removed from the grain boundary and the diffusion controlled process is limited by the rate of diffusion of the slowest participant (in this case Ni).

The annealing of dislocation loops is also dependent upon the diffusion of vacancies through the matrix. However, the stacking fault energy and line tension of the dislocation loop also influence the annealing process by reducing the energy barrier required for removal. Accounting for the stacking fault energy and line tension results in an apparent activation energy for loops which is 0.6 to 0.15 eV lower than that for RIS for loops ranging in size from 1 to 20 nm, respectively. The apparent activation energy for loops determined from Figure 5 is 2.5 eV or 0.6 eV lower than that for removal of RIS.

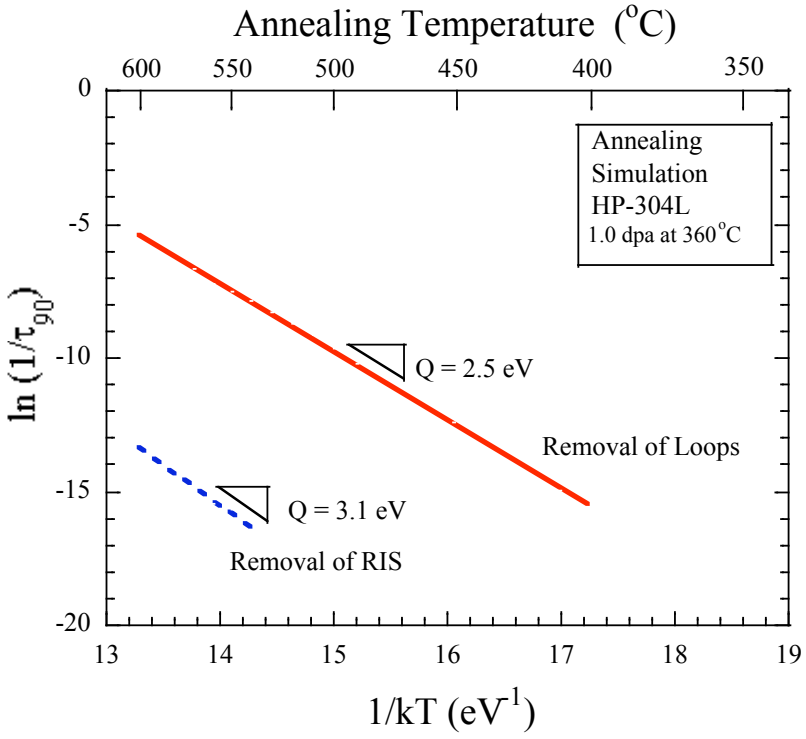

Figure 5: Comparison of activation energies for removal of dislocation loops and RIS during simulated post-irradiation anneal of HP-304L irradiated to 1.0 dpa at 360°C.

4.1.3 Kinetic considerations

Although, thermodynamics are important in the annealing processes, kinetic factors may also play a role. The pre-exponential term in Eq. (6) is also of interest and was also determined to be 2.2 x 10^{12} s^{-1} for loops and 1.1 x 10^{12} s^{-1} for RIS. The difference in pre-exponential terms also gives insight into the importance of the density of defects required for annealing to be discussed in the next section. Consider the case where annealing is performed at extremely high temperatures (where 1/kT approaches 0). In this regime, an infinite, inexhaustible supply of vacancies is available for annealing of both RIS and loops. Yet, a difference in removal rates still exists, implying kinetics are an important consideration at low temperatures.

The most straightforward comparison between loop and RIS annealing kinetics is the number of vacancies required to remove a population of dislocation loops versus that for removal of the segregation profiles. Since the nature of the two irradiation-induced features is different,

comparisons of the number of vacancies to remove them must be made on a common scale, such as the number of defects per unit volume.

A 10.5 nm interstitial dislocation loop lying on the (111) plane is a conglomeration of ~3200 interstitials. Therefore, to remove this loop entirely, a net of 3200 vacancies must be absorbed at each loop. Given a dislocation density of 4.9×10^{15} loops/cm^3, a total of 1.6×10^{19} vacancies/cm^3 are required to completely remove the dislocation loop population.

The number of vacancies required to remove the segregation profiles per cm^3 can also be calculated. The MIK code was used to track the number of vacancies passing a marker plane set at 10 nm (maximum width of RIS profile after 1.0 dpa at 360°C). The number of vacancies was then integrated over time until the segregation profile was completely removed. For the profiles typical of 1.0 dpa irradiation, a minimum of 3.8×10^7 vacancies per 100 nm^2 of grain surface area are required to remove the segregation profiles. For 11.5 μm grains, there are approximately 5200 cm^2 of grain boundary area per cm^3. Thus, a total of 2.0×10^{23} vacancies/cm^3 are required to completely remove the segregation profiles. Comparison of the number of vacancies required for removal indicates that a factor of 2×10^4 more vacancies per cm^3 are required to remove the segregation profiles than the dislocation densities. Clearly, since fewer vacancies are required to remove dislocation loops than RIS profiles, equal defect fluxes to each sink will result in more rapid removal of dislocation loops.

Since grain boundaries and dislocation loops are both defect sinks, they may also compete for the same thermal vacancies during annealing. Specifically, if a vacancy traveling to a grain boundary passes other sinks, the probability that it reaches the grain boundary is greatly reduced. Grain boundaries act as a planar sink for defects created throughout the grain, while the dislocation loop population is a series of sinks spread throughout the grain. Note, however, that only those vacancies relatively close to the grain boundary will be influenced by the solute composition gradient and move towards the boundary to participate in annealing. The width of the vacancy concentration profile during post-irradiation annealing was investigated using the MIK code. During annealing at 500°C, the vacancy concentration returns to the equilibrium concentration ~220 nm away from the grain boundary. Therefore, within ~200 nm of the grain boundary, the boundary and loops in this region compete for vacancies, while in regions more than 200 nm away, loops are the only sink for vacancies.

For the CP-304 SS at 1.0 dpa, the mean loop size is 4.9 nm and the density was 17.0 x 10^{21} m^{-3}. For a homogeneously distributed population, the distance between loops is, on average, ~110 nm. In this situation, a diffusing vacancy may encounter more than one dislocation loop over its diffusion path towards the grain boundary, increasing the likelihood that it will be absorbed at a loop rather than a grain boundary. Another MIK simulation was performed to evaluate the influence of the dislocation loop density on annealing of RIS profiles. Simulations of annealing at 500°C were performed with both the as-irradiated dislocation density and with no loops. The results for the two simulations are compared in Figure 6. Clearly, reducing the dislocation density increases the rate of annealing of RIS, which confirms that loss of vacancies to competing sinks such as dislocation loops reduces the annealing rate of RIS.

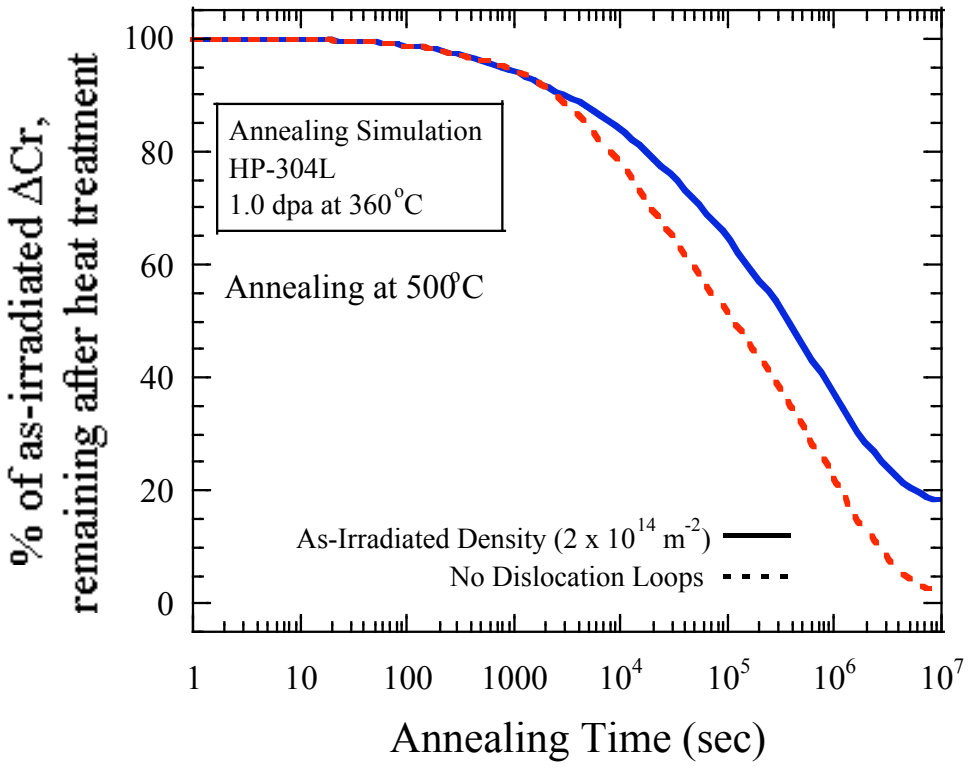

Figure 6: Simulation of annealing of Cr segregation as a function of time during post-irradiation annealing at 500°C. Simulation with as-irradiated dislocation density and no dislocation density.

In summary, the preferential removal of dislocation loops can be explained by considering both thermodynamic and kinetic factors. Calculation of the apparent activation energy, the density of defects required for annealing, and potential competition between loops and RIS for thermal vacancies all support the preferential removal of dislocation loops during post-irradiation annealing.

4.2 Post-Irradiation Annealing: Experimental Results

4.2.1 RIS

During post-irradiation annealing, the degree of Cr depletion did not change significantly from the irradiated condition until the most extreme annealing conditions for either the HP-304L at 1.0 dpa or the CP-304 at 1.0 and 2.5 dpa. Similarly, the amount of Ni and Fe segregation did not change appreciably. However, for the CP-304 alloy the enrichment of minor elements such as Si and P was removed rapidly with annealing.

HP-304L

The results of composition measurements on samples of the HP-304L irradiated to 1.0 dpa in the as-irradiated condition and the post-irradiation annealed condition are listed in Table 2. (in at%). The number of measurements for each condition is given in the left-most column. Typical Cr segregation profiles for each annealing condition are shown in Figure 7 a.). All plots in Figure 7 a.) also contain the as-irradiated profile (shown as open symbols) for direct comparison. Grain boundary Cr depletion remained virtually unchanged with annealing treatments below treatments of 600°C/45 min. Annealing at 600°C/90 min. removed, on average, only 17% of the as-irradiated depletion (17.4 at% versus 16.4 at% in the as-irradiated case) and resulted in little change to the shape of the segregation profile while annealing at 650°C/45 min. removed 66% of the as-irradiated Cr depletion.

Similarly, the amount of grain boundary Ni enrichment also remained virtually unchanged with annealing treatments up to 650°C/45 min., which removed virtually all as-irradiated Ni enrichment. The measured grain boundary Fe enrichment remained at or above the amount measured in the as-irradiated condition (2.5 at% enrichment) with annealing treatments up to

annealing treatments of 600°C/45 min. Further annealing removes additional Fe enrichment, with the grain boundary Fe content dropping to 70.4 at% (1.4 at% enrichment after annealing at 650°C/45 min.).

Table 2: Summary of grain boundary composition measurements on post-irradiation annealed HP-304L (irradiated to1.0 at 360°C). All results are listed in at%.

Irradiation Condition	Fe	Cr	Ni	Mn
HP-304L matrix/bulk comp.	69.0	20.9	9.0	1.1
As-irradiated-1.0 dpa				
GB avg. (25 meas.)	71.5	16.4	11.4	0.72
Std. Dev. Of mean (at%)	0.2	0.3	0.2	0.03
500°C/45 min.				
GB avg. (28 meas.)	72.1	16.1	11.1	0.75
Std. Dev. Of mean (at%)	0.2	0.2	0.2	0.02
500°C/300 min.				
GB avg. (8 meas.)	72.5	16.1	10.8	0.71
Std. Dev. Of mean (at%)	0.5	0.3	0.3	0.04
550°C/45 min.				
GB avg. (9 meas.)	71.7	16.6	10.9	0.79
Std. Dev. Of mean (at%)	0.5	0.4	0.3	0.06
600°C/45 min.				
GB avg. (18 meas.)	72.1	15.4	11.8	0.75
Std. Dev. Of mean (at%)	0.2	0.3	0.4	0.04
600°C/90 min.				
GB avg. (26 meas.)	71.0	17.2	10.8	0.96
Std. Dev. Of mean (at%)	0.2	0.1	0.2	0.05
650°C/45 min.				
GB avg. 13 meas.)	70.4	19.4	9.2	0.96
Std. Dev. Of mean (at%)	0.5	0.6	0.4	0.05

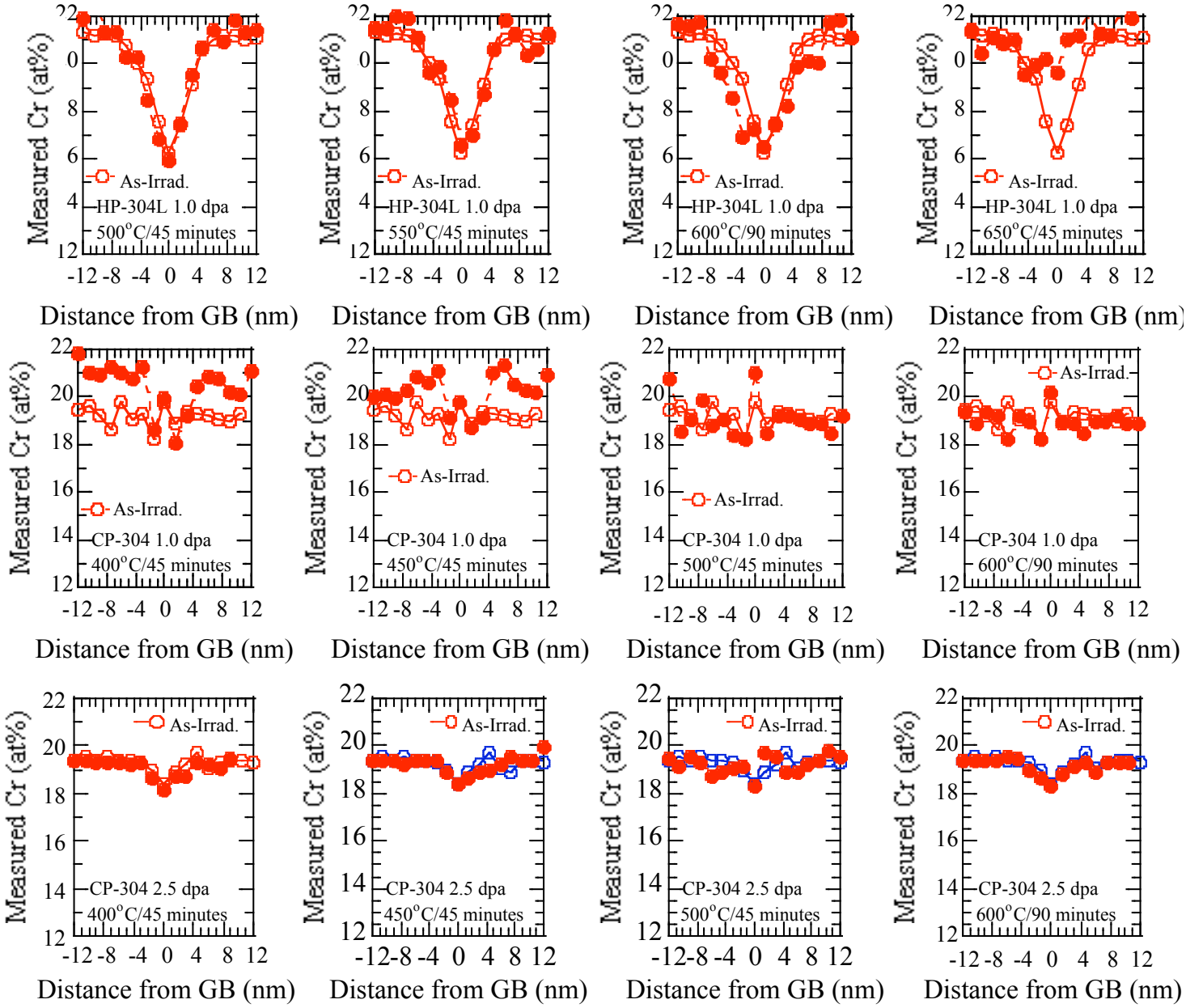

Figure 7. Cr segregation profiles following irradiation with 3.2 MeV protons at 360°C and post-irradiation annealing: HP-30L to 1.0 dpa and CP-304 to 1.0 dpa and 2.5 dpa. The as-irradiated profile is shown by the open symbol. The 0 nm position is the grain boundary for all profiles.

CP-304

The composition measurements for the CP-304 samples irradiated to 1.0 and 2.5 dpa in both the as-irradiated and post-irradiation annealed conditions are summarized in Table 3. (in at%) and shown in Figures 7 b.) and 7 c.) for the 1.0 and 2.5 dpa samples, respectively. At 1.0

dpa, both the degree of Cr depletion and shape of the Cr segregation profiles remained virtually unchanged for all annealing treatments. In the as-irradiated condition, the Cr segregation profile has a "w-shape", that is, the minimum in composition is on either side of the grain boundary with a local maximum in concentration at the grain boundary. Following anneals at 400°C, 450°C, and 500°C for 45 min., the minimum in measured Cr content near the grain boundary is unchanged from the as-irradiated level. The Cr content at the grain boundary Cr content increased slightly with annealing, although, the as-irradiated and all annealed GB Cr contents at the peak of the "w-shape" were measured at levels above the bulk content. Of more significance is that the complex, "w-shape" segregation profiles remained unchanged. Even annealing at 600°C/90 min., did not alter the as-irradiated GB Cr content or the segregation profiles. Similarly, the amount of grain boundary Ni enrichment remained unchanged with all annealing treatments while the degree of grain boundary Fe depletion was slightly altered with all annealing treatments as listed in Table 3.

Contrary to Cr, Fe, and Ni, grain boundary Si changes significantly during post-irradiation annealing as shown in Table 3. The grain boundary Si enrichment was reduced steadily with annealing, with only 0.2 at% enrichment remaining after annealing at 600°C/90 min. Grain boundary P also changes drastically during post-irradiation annealing. Following annealing at 400°C/45 min., the grain boundary P content has dropped to nearly the bulk level (from 1.47 at% in the as-irradiated condition) where it remains for all other annealing treatments.

For the samples irradiated to 2.5 dpa, the grain boundary Cr profiles remained virtually unchanged with all annealing treatments. Contrary to the 1.0 dpa case the higher dose produces a more traditional "v-shape" profile and a higher degree of Cr depletion. Annealing at 600°C for 90 min. did not alter the as-irradiated GB Cr content or the segregation profiles for the CP-304 irradiated to 2.5 dpa as illustrated in Figure 7c.). The grain boundary Ni and Fe content remained relatively unchanged from the as-irradiation condition, similar to the 1.0 dpa samples.

Similar to the 1.0 dpa case, grain boundary Si changed significantly during post-irradiation annealing with the grain boundary Si content dropping significantly with increasing annealing time or temperature with only 0.3 at% enrichment remaining after annealing at 600°C/90 min. Grain boundary P also changed drastically during post-irradiation annealing. Following annealing at 400°C for 45 min., the grain boundary P content dropped to 0.46 at%

from 1.47 at% in the as-irradiated condition. All other treatments resulted in grain boundary P contents near the bulk level of 0.055 at%.

Table 3: Summary of grain boundary composition measurements* on post-irradiation annealed CP-304 (irradiated to1.0 and 2.5 dpa at 360°C). All results are listed in at%.

Irradiation Condition	Fe*	Cr*	Ni	P	Mo*	Mn	Si
CP-304 matrix/bulk comp.	69.4	19.3	7.9	0.055	0.21	1.40	1.27
As-irradiated 1.0 dpa							
GB avg. (50 meas.)	66.7/68.2	19.6/18.5	8.6	1.47	0.41/0.22	1.09	2.14
Std. Dev. Of mean	0.2/0.2	0.1/0.1	0.1	0.01	0.02/0.02	0.05	0.02
400°C/45 min.							
GB avg. (10 meas.)	67.9/68.9	19.8/18.6	8.7	0.08	0.41/0.35	1.27	1.85
Std. Dev. Of mean	0.5/0.5	0.3/0.3	0.2	0.01	0.1	0.11	0.05
450°C/45 min.							
GB avg. (20 meas.)	67.9/69.1	20.2/18.6	8.5	0.07	0.27/0.27	1.18	1.79
Std. Dev. Of mean	0.3/0.3	0.3/0.3	0.2	0.01	0.01	0.11	0.05
500°C/45 min.							
GB avg. (21 meas.)	67.4/69.5	20.9/18.9	8.5	0.07	0.27/0.23	1.17	1.67
Std. Dev. Of mean	0.3/0.3	0.2/0.2	0.1	0.01	0.02/0.02	0.02	0.05
600°C/90 min.							
GB avg. (10 meas.)	67.9/69.2	20.3/18.8	8.9	0.06	0.22/0.22	1.13	1.47
Std. Dev. Of mean	0.2/0.2	0.1/0.1	0.2	0.01	0.01/0.01	0.07	0.06
As-irradiated 2.5 dpa							
GB avg. (20 meas.)	66.8	18.4	9.7	1.47	0.35	0.85	2.42
Std. Dev. Of mean	0.2	0.2	0.2	0.03	0.03	0.05	0.05
400°C/45 min.							
GB avg. (10 meas.)	68.0	18.3	9.9	0.46	0.33	1.00	2.02
Std. Dev. Of mean	0.3	0.1	0.2	0.01	0.1	0.04	0.05
450°C/45 min.							
GB avg. (13 meas.)	68.2	18.4	9.7	0.08	0.31	0.82	1.95
Std. Dev. Of mean	0.5	0.1	0.3	0.01	0.05	0.05	0.07
500°C/45 min.							
GB avg. (21 meas.)	68.8	18.4	9.8	0.07	0.25	0.83	1.77
Std. Dev. Of mean	0.3	0.1	0.2	0.01	0.01	0.03	0.05
600°C/90 min.							
GB avg. (14 meas.)	68.8	18.3	9.7	0.07	0.22	0.91	1.57
Std. Dev. Of mean	0.4	0.1	0.3	0.02	0.02	0.06	0.08

*Average at GB/Max (Min) segregation measured adjacent to boundary for "W-shaped" profiles.

The removal of Cr segregation for the HP-304L and CP-304 irradiated to 1.0 and 2.5 dpa is plotted in Figure 8 as a function of Fe-diffusion distance. Because both time and temperature were varied, the diffusion distance of Fe was chosen as a single variable which combines both time and temperature effects. The diffusion distance is equal to $(D_{Fe}t)^{1/2}$ where t is annealing time and D_{Fe} is diffusivity for Fe at the annealing temperature. Also plotted in Figure 8 are the results from experimental studies of Jacobs et al. [37], Katsura et al. [38], and Bruemmer et al. [39] for CP-304 and 316 irradiated to ~1.0 dpa. For alloys and doses where a "w-shape" profile was observed, the percent of the minimum measured value remaining is plotted. Note that for conditions where the amount of Cr segregation *increased* with annealing, the percentage remaining is plotted as 100%. This is most significant in the data of Bruemmer where a CP-316 alloy with an extremely sharp "w-shape" profile was measured. The Cr content measured in the as-irradiated case was above the bulk level and continued to increase above the bulk level during post-irradiation annealing. Overall, the data from this study and other studies are in excellent agreement. Only two annealing conditions (HP-304L at 650°C/45 min. and Katsura's CP-316 at 650°C/1 h) resulted in the Cr segregation being less than 80% of the as-irradiated value.

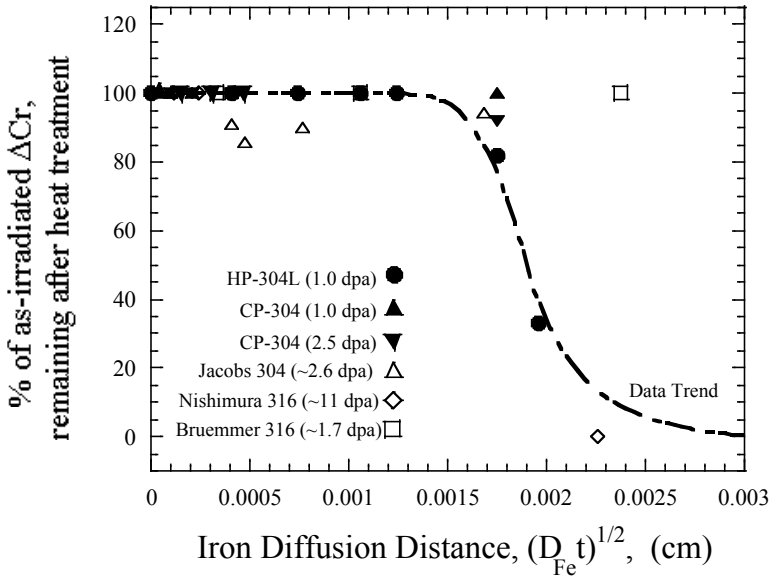

Figure 8. Annealing of Cr segregation as a function of Fe-diffusion distance. The % of as-irradiated *minimum* measured Cr is plotted for all conditions. Data points for CP-304 at 1.0 dpa and 2.5 dpa have been shifted left and right, respectively, for clarity.

In Figure 9, the experimental data are compared to the predictions of the MIK model. The model predictions are plotted as a function of the measured result from both this study and available literature data. When plotted in this fashion, model and measured results can be compared for all available data. A line with a slope of unity was applied to the data set (shown in Figure 9), resulting in a correlation coefficient of 0.85. A line with slope = 1 represents a one-to-one correlation between modeled and measured results. However, the most significant differences between the simulation and measured data occur where the measurements show no change in the as-irradiated Cr depletion. For these data points the model clearly overpredicts the rate of annealing. The majority of these data points are for conditions containing "w-shape" profiles (CP-304 at 1.0 dpa and CP-316 data from Bruemmer), which the MIK model is not capable of simulating accurately [40]. Excluding these points from the statistical analysis improves the correlation coefficient to 0.93.

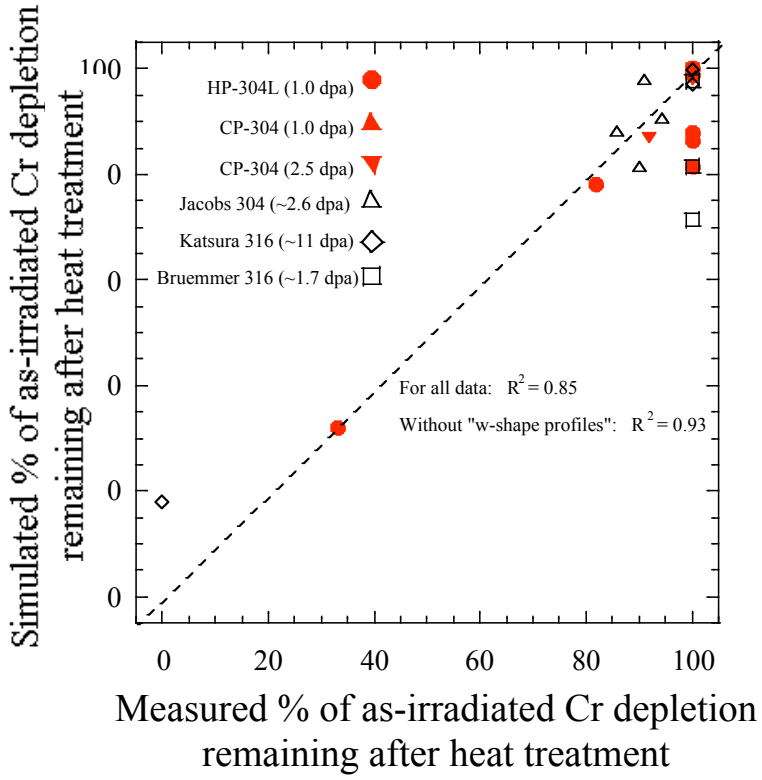

Figure 9. Comparison of measured annealing of Cr segregation with simulated annealing using the MIK model.

Grain boundary segregation of Si and P is removed much faster than Cr or Ni for the same annealing treatments. For both the 1.0 and 2.5 dpa CP-304 samples, the as-irradiated enrichment of Si, and P are all significantly affected by annealing at 400°C for 45 min., contrary to the observed annealing of Cr and Ni. The more rapid removal of Si segregation during post-irradiation annealing can be explained by considering the tracer impurity diffusion coefficients [41]. Silicon diffuses considerably faster than Cr or Ni. Coupled with a considerable Si enrichment in the 1.0 and 2.5 dpa condition (1.7 and 1.9 times bulk content, respectively), Si enrichment should be removed rapidly during post-irradiation annealing. Phosphorous also diffuses via vacancies in Fe-Cr-Ni alloys [42], although the diffusion coefficients are less well known than those for the major and other minor alloying elements. Nonetheless, in the as-irradiated 1.0 and 2.5 dpa condition, P is enriched a factor of 27 times over the bulk content (1.47 at% for both 1.0 and 2.5 dpa versus a bulk content of 0.055 at%). The extreme concentration gradient in the as-irradiated condition can explain the very rapid removal of P enrichment during post-irradiation annealing.

4.2.2 Dislocation loops

During post-irradiation annealing, dramatic changes were measured in the dislocation loop population. For the HP-304L at 1.0 dpa and CP-304 to 1.0 and 2.5 dpa, the dislocation loop density decreased steadily with increasing annealing time or temperature while the mean dislocation size remained relatively unchanged. The mean loop diameters and loop densities were determined for each annealing condition and are summarized in Table 4 for both alloys. Bright field images of the dislocation population before and after annealing are shown in Figure 10.

HP-304L

For the HP-304L, in the as-irradiated condition, the mean loop diameter was 11.0 nm. Annealing at 500°C for 45 min. resulted in a slightly smaller mean diameter (10.8 nm) while anneals at 600°C for 45 min., and 600°C for 90 min. both resulted in a slightly larger loop diameter (11.7 and 12.1 nm, respectively). Bright field images of the dislocation loops in both

the as-irradiated and annealed conditions are shown in Figure 10a. Some dislocation loops that have unfaulted and grown (not discriminated by the bright field imaging) may have contributed to this measured growth. Also, the simulations predicted the preferential removal of small loops from the population that would also result in an apparent growth in mean loop diameter.

Table 4. Summary of dislocation loop analysis on post-irradiation annealed HP-304L and CP-304 (irradiated to 1.0 and 2.5 dpa at 360°C).

Annealing temp. (°C)	Annealing time (min.)	Mean loop diameter (nm)	Loop density x 10^{21} (# /m^3)	Total loop line length x 10^{14} (m/m^3)	% As-irradiated line length remaining
HP-304L 1.0 dpa					
As-irradiated		11.0	5.6	1.94	100.0
500	45	10.8	4.2	1.43	73.6
600	45	11.7	1.9	0.69	36.1
600	90	12.1	0.16	0.06	3.1
650	45	9.2	0.14	0.04	2.1
CP-304 1.0 dpa					
As-irradiated		4.9	17.0	2.61	100.0
400	45	4.8	18.0	2.71	100.0
450	45	5.6	16.5	2.90	100.0
500	45	5.8	12.0	2.19	83.8
600	90	6.7	0.29	0.06	2.4
CP-304 2.5 dpa					
As-irradiated		5.2	40.0	6.53	100.0
400	45	5.4	38.7	6.56	100.0
450	45	5.4	37.1	6.29	96.4
500	45	5.8	18.7	3.41	52.2
600	90	6.1	0.96	0.18	2.8

Alternatively, a portion of the dislocation loop population may, indeed, be composed of vacancy-type dislocation loops, that will grow with annealing. Computer simulation of the post-irradiation annealing of both vacancy and interstitial type dislocation loops by Simonen et al. [43] suggests that both the presence of vacancy-type loops in a loop population and their growth during annealing are feasible. Only annealing at 650°C/45 min. resulted in a loop size significantly smaller (9.2 nm) than the as-irradiated value. Contrary to the mean loop diameter, the dislocation loop density dropped significantly during annealing. In the as-irradiated condition, a loop density of 5.6 x10^{21}m^{-3} was measured, which was steadily reduced with annealing. Following the most severe annealing condition (650°C for 45 min) a density of only 0.14 x10^{21}m^{-3} remained.

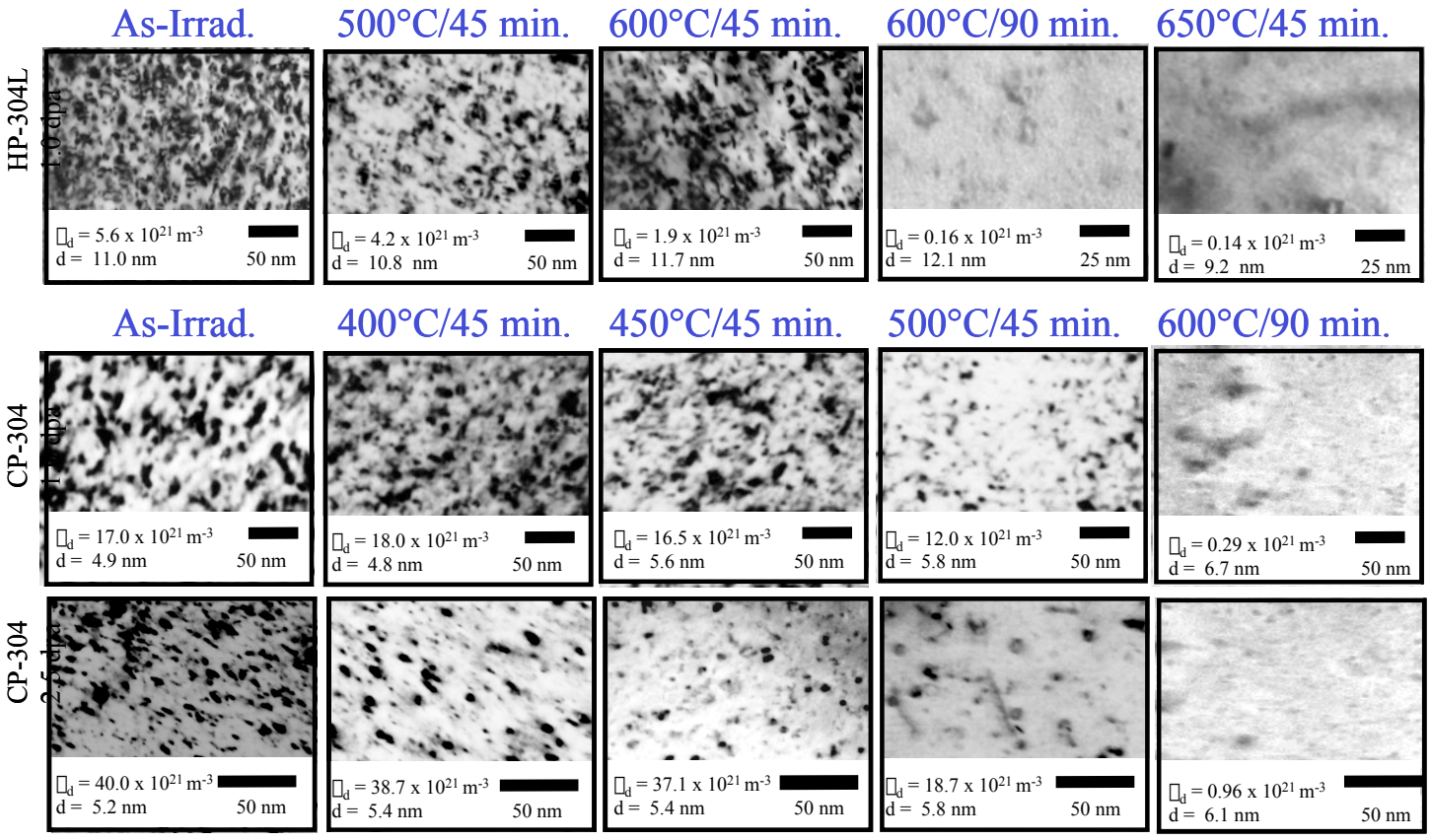

Figure 10. Bright field images of dislocation loop populations in HP-304L and CP-304 irradiated with 3.2 MeV protons at 360°C to 1.0 dpa and 2.5 dpa and post-irradiation annealed.

CP-304

For the CP-304 irradiated to 1.0 dpa and annealed, the very dense dislocation population in the as-irradiated condition is steadily reduced with annealing, as indicated in the bright field images shown in Figure 10b. In the as-irradiated condition, the mean loop diameter was 4.9 nm, but at a density of 17.0 $x10^{21}m^{-3}$. During annealing, the mean loop diameter increased slightly (up to 6.7 nm after 600°C/90 min). The dislocation loop density steadily decreased during increased annealing time or temperature. Following annealing at 600°C for 90 min., very few loops were observed.

Bright field images of the dislocation population following proton irradiation of the CP-304 to 2.5 dpa and subsequent annealing are also shown in Figure 10. As in the samples irradiated to 1.0 dpa, the very dense dislocation population in the as-irradiated condition is steadily removed with annealing. The mean loop size grew from the as-irradiated diameter of 5.2 nm to 6.1 nm following annealing a 600°C/90 min anneal. Loop density dropped from the as-irradiated density of 40.0 $x10^{21}m^{-3}$ to 0.96 $x10^{21}m^{-3}$ after the same 600°C/90 min anneal.

The behavior of the dislocation microstructure during post-irradiation annealing of the CP-304 alloy in this study is summarized in Figure 11. Also plotted are the results for neutron-irradiated 304SS by Jacobs et al. [37]. The total dislocation line length associated with the dislocation loop population is plotted as a function of Fe-diffusion distance. The loop line length from the proton-irradiated samples is removed steadily with increasing annealing time or temperature. Jacob's data, however, are somewhat contradictory. The two data points from the neutron-irradiated samples indicate that the line length actually increases during annealing. Jacobs measured a large increase in loop diameter (6.7 to 10.7 nm) for the anneal at a diffusion distance of 0.0017 cm (475°C for 24 h) and attributed this discrepancy to the unfaulting of dislocation loops which artificially increased the mean loop diameter.

The experimental data of both this study and that of Jacobs are compared to the dislocation loop-annealing model in Figure 12. The simulated results are plotted as a function of measured results for each experimental data point in this study and available data from other studies. A line with a slope of one is also plotted in Figure 10. This line fits the data set with a correlation coefficient of 0.92. As with the comparison of RIS annealing shown in Figure 9, there is no systematic difference between measured and model results.

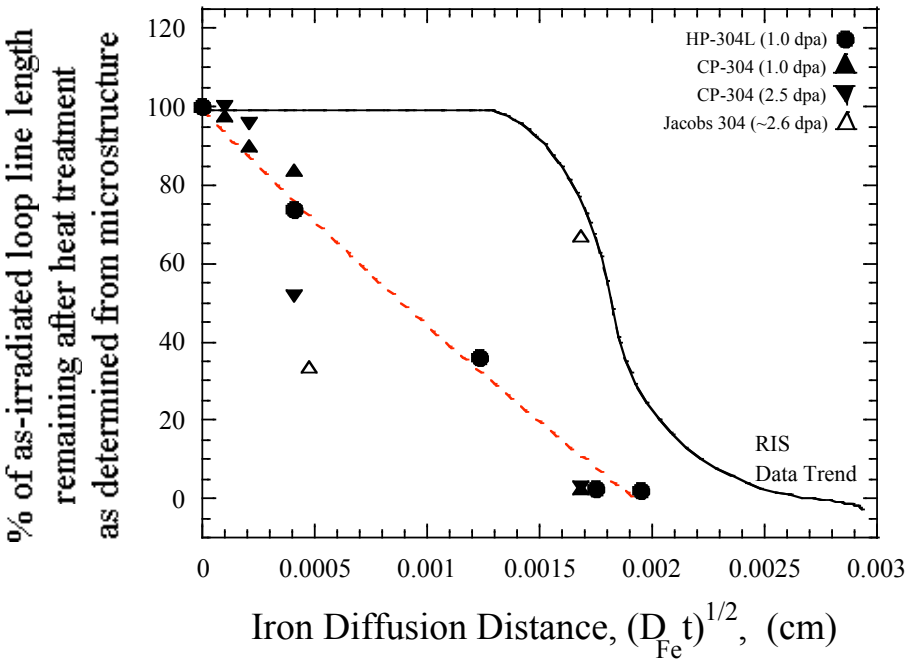

Figure 11. Annealing of dislocation microstructure as a function of Fe-diffusion distance. The fraction of the as-irradiated loop line length associated with the dislocation population is plotted.

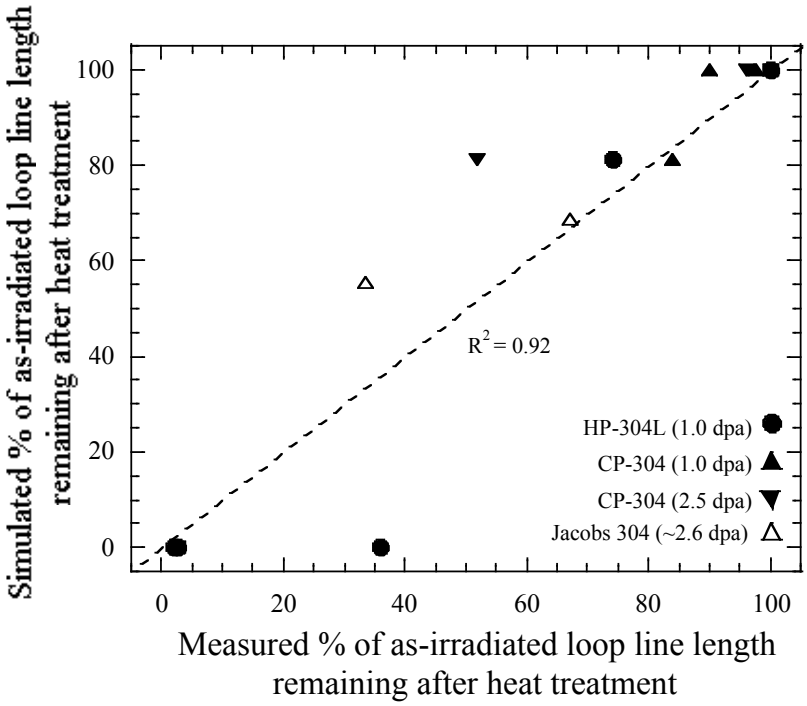

Figure 12. Comparison of simulated and measured annealing of dislocation loop line length.

However, comparison of the measured loop sizes with the simulated results reveals a discrepancy. The loop annealing model predicts that the mean loop size will shrink steadily during annealing while experimental results show that the loop size remains constant or increases slightly during annealing up to anneals at 600°C for 90 min., beyond which the loop radius decreases. Thus, in order for the simulated change in yield stress to match the experimental values, the model must underpredict the change in loop density to compensate for the overprediction of change in loop radius. This discrepancy may be explained by the unfaulting of dislocation loops during annealing, as noted by Jacobs. Dislocation loops that unfault are free to grow or glide and will behave differently during post-irradiation annealing. According to Olander [44], unfaulting is very slow at temperatures below ~550°C, but dislocation loops may spontaneously unfault at temperatures above 600°C. Since the bright field imaging technique used in this study images both faulted and unfaulted dislocation loops, the reported diameter and density may have been determined from a population containing some unfaulted dislocation loops, similar to the experience of Jacobs. The dark-field rel-rod technique images only faulted dislocation loops and could resolve this issue. However, the rel-rod technique is extremely hard to use to image very low dislocation densities, which is why the bright field technique was used exclusively in this study.

4.2.3 Hardness

As with dislocation loop density, the measured hardeness decreases steadily with increasing annealing time or temperature for both the HP-304L and the CP-304 (at both 1.0 and 2.5 dpa). Table 5 lists the results of the hardness measurements for both the as-irradiated and annealed specimens. For the HP-304L alloy irradiated to 1.0 dpa, a hardness of 229 kg/mm^2 (62 kg/mm^2 above the unirradiated value) was measured. After annealing at 500°C for 45 min. hardness was reduced to 212 kg/mm^2 (a 28.5% reduction in radiation-induced hardness). Increased annealing temperature resulted in an increased removal of radiation-induced hardening. After annealing at 600°C /90 min. or 650°C/45 min. all radiation-induced hardening was removed.

Table 5: Summary of hardness analysis on post-irradiation annealed CP-304 (irradiated to 1.0 and 2.5 dpa at 360°C).

							From Hardness		From Loops	
Anneal temp. (°C)	Anneal. time (min.)	Unirrad H_v (kg/mm^2)	As-irrad H_v (kg/mm^2)	As-irrad. ΔH_v (kg/mm^2)	Annealed H_v (kg/mm^2)	Annealed ΔH_v (kg/mm^2)	$\Delta\sigma_y$ (MPa)	% As-Irrad. $\Delta\sigma_y$ remain.	$\Delta\sigma_y$ (MPa)	% As-irrad. $\Delta\sigma_y$ remain.
HP-304L 1.0 dpa										
As-irradiated		167	229	62	229	62	219.8	100.0	186.2	100.0
500	45	167	223	56	212	45	159.6	72.5	159.8	85.8
500	300	167	234	67	207	40	141.8	59.7	--	--
550	45	167	234	67	217	50	177.3	74.6	--	--
600	45	167	224	57	182	15	53.2	24.2	111.8	60.1
600	90	167	250	83	166	-1	-3.5	-1.2	33.0	17.7
650	45	167	255	88	156	-11	-39.0	-12.5	26.9	14.5
CP-304 1.0 dpa										
As-irradiated		220	270.5	50.5	270.5	50.5	179.1	100.0	227.5	100.0
400	45	220	270.5	50.5	273.0	53.0	187.9	105.0	223.4	98.2
450	45	220	270.5	50.5	273.7	53.7	190.4	106.3	215.9	94.9
500	45	220	270.5	50.5	266.4	46.4	164.5	91.9	207.9	91.4
600	90	220	270.5	50.5	228.8	8.8	31.2	17.4	36.8	16.2
650	45	220	270.5	50.5	218.9	-1.1	3.9	-2.2	--	--
CP-304 2.5 dpa										
As-irradiated		220	326.0	106.0	326.0	106.0	375.9	100.0	359.5	100.0
400	45	220	326.0	106.0	320.8	100.8	357.4	95.1	360.1	100.0
450	45	220	326.0	106.0	316.1	96.1	340.8	90.6	352.6	98.0
500	45	220	326.0	106.0	290.8	70.8	251.1	66.8	259.9	72.0
600	90	220	326.0	106.0	234.3	13.4	47.5	12.6	60.0	16.7

For the CP-304 alloy in the 1.0 dpa as-irradiated condition, a hardness of 271 kg/mm^2 (51 kg/mm^2 above the unirradiated value of 220 kg/mm^2) was measured by Was et al. [29] and confirmed in this study. After annealing at 400°C/45 min. and 450°C/45 min., the hardness remained at the as-irradiated level. However, annealing at 600°C/90 min. removed almost all the as-irradiated hardness increase. Similarly, for the 2.5 dpa samples, annealing at 400°C/45 min. and at 450°C/45 min. the hardness was not significantly different from the as-irradiated level, while annealing at 600°C/90 min. removed a more significant portion of the radiation-induced hardening (only 16.7% remaining).

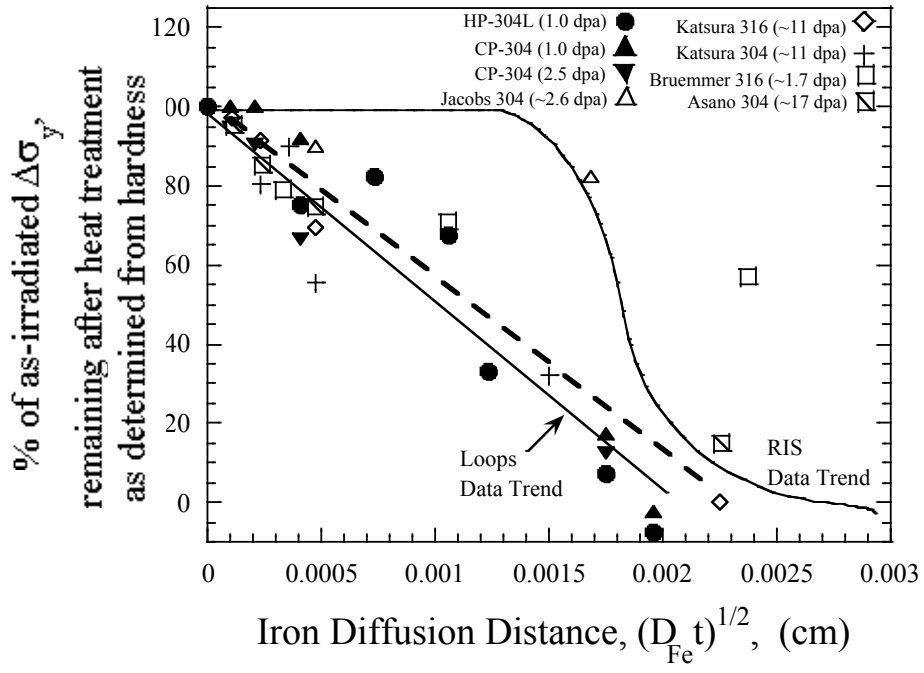

Figure 13: Annealing of measured hardness as a function of Fe-diffusion distance. The fraction of the as-irradiated change in yield stress calculated from hardness measurements is plotted.

The fraction of radiation-induced yield stress change calculated from hardness measurements is plotted as a function of Fe-diffusion distance in Figure 13 for both the CP304 irradiated to 1.0 and 2.5 dpa and the HP-304L of this study. The results from studies by Jacobs, Asano, Bruemmer, and Katsura on 304 SS and Katsura on 316 SS are also plotted. With the

exception of single data points from Bruemmer and Jacobs each, the hardness decreases steadily with increasing annealing time and temperature for all alloys. Further, the data from this study are in excellent agreement with that from Jacobs [37], Katsura [138], and Bruemmer [39]. However, more importantly, all the data from hardness measurements follow the same trend during annealing and are also in excellent agreement with that calculated from microstructure measurements.

4.2.4 IASCC of Post-Irradiation Annealed Stainless Steel

The strain to failure and extent of intergranular cracking changed dramatically during post-irradiation annealing for both 1.0 and 2.5 dpa CP-304 samples tested in the water environment. The strain-to- failure and measured ultimate tensile strength (UTS), as well as the location and nature of failure for each specimen in CERT tests of the 1.0 and 2.5 dpa samples are summarized in Table 6. With annealing, the strain-to-failure increases with increasing diffusion distance for both 1.0 and 2.5 dpa samples. The 1.0 dpa sample annealed at 400°C for 45 min. failed at 23.3%, close to the strain-to-failure of the as-irradiated specimens, while all other annealed 1.0 dpa samples failed at ~30% strain, which is more representative of the 0.3 dpa samples of the same alloy which failed via ductile rupture [29]. Similarly, the strain-to-failure for the 2.5 dpa sample annealed at 400°C for 45 min. was 26.5% while the sample annealed at 500°C for 45 min. failed at 33.7% strain.

All four 1.0 dpa specimens failed in the unirradiated region or the threads of the sample. All faces of each specimen and the fractured ends were examined in detail for evidence of IG cracking. The 1.0 dpa samples annealed at 400°C for 45 min. and 450°C for 45 min. both had one crack on the irradiated face of the specimen, approximately 250 mm long and IG in nature. This is approximately the same length of IG cracking observed on the fractured end in the 1.0 dpa as-irradiated specimens strained under the same conditions [29]. For the samples annealed at 500°C/45 min. and the 600°C/90 min., no cracks were found on any of the sample surfaces. All four of the post-irradiation annealed 2.5 dpa samples failed in the irradiated region. The samples annealed at 400°C and 450°C for 45 min. both exhibit a fracture morphology similar to the 3.0 dpa as-irradiated fracture morphology. In addition to the crack leading to failure, 2 and 6 additional cracks were found on the irradiated surface for the samples annealed at 400°C and

450°C, respectively. Contrary to the samples annealed at 400°C and 450°C for 45 min., the sample annealed at 500°C/45 min. failed entirely via ductile rupture. Finally, the 2.5 dpa sample annealed at 600°C/90 min. exhibited extensive IG cracking on all four faces of the sample, not just the irradiated face, similar to that observed in sensitized specimens. Cookson [45] tested a sensitized HP-304L sample (650°C for 24 h) under identical water conditions and observed almost 100% IG failure at only 11.5% strain (compared to 30% strain-to-failure for unirradiated specimens), suggesting that the 2.5 dpa sample may have actually been annealed at temperature higher than 600°C and sensitized (potentially due to a thermocouple failure).

Table 6. Summary of CERT test results performed on post-irradiation annealed CP-304 samples (1.0 and 2.5 dpa).

Annealing temp. (°C)	Annealing time (min.)	Strain at failure (%)	UTS (ksi)	Location of failure	Number of cracks in irradiated region	Total crack length on irradiated surface (μm)[#]
CP-304 1.0 dpa						
--	--					
400	45	23.3*	62.1**	Unirrad. region	1	270
450	45	30.0*	NA	Unirrad. region	1	234
500	45	30.6	66.6	Threads	0	0
600	90	30.6	75.8	Near shoulder	0	0
CP-304 2.5 dpa						
400	45	26.5	60.3	Irrad. region	3	1540
450	45	22.7	59.1	Irrad. region	7	3540
500	45	33.7	64.0	Irrad. region	0	0
600	90	10.8	40.5	Irrad. region	0	0

[#]Sum of length of all regions characterized as IG or TG, including crack that led to failure.
*ESTIMATED DUE TO LOAD CELL FAILURE PRIOR TO SAMPLE FAILURE. ± 0.5%
**Maximum measured before load cell failed.

The percentage of as-irradiated crack length remaining after post-irradiation annealing is plotted in Figure 14. Even the lowest temperature anneal reduced the crack length relative to the as-irradiated level. Annealing at 500°C for 45 min. and above removed all evidence of IG cracking in both the 1.0 dpa and 2.5 dpa samples. The rapid and distinct change in cracking mode from clearly IG after annealing at 450°C to completely ductile after annealing at 500°C is also shown in Figure 14. The cracking results of this study are in good agreement with the cracking response measured by Jacobs [37] and Katsura [38] on neutron-irradiated and annealed 304 and 316 stainless steels, respectively.

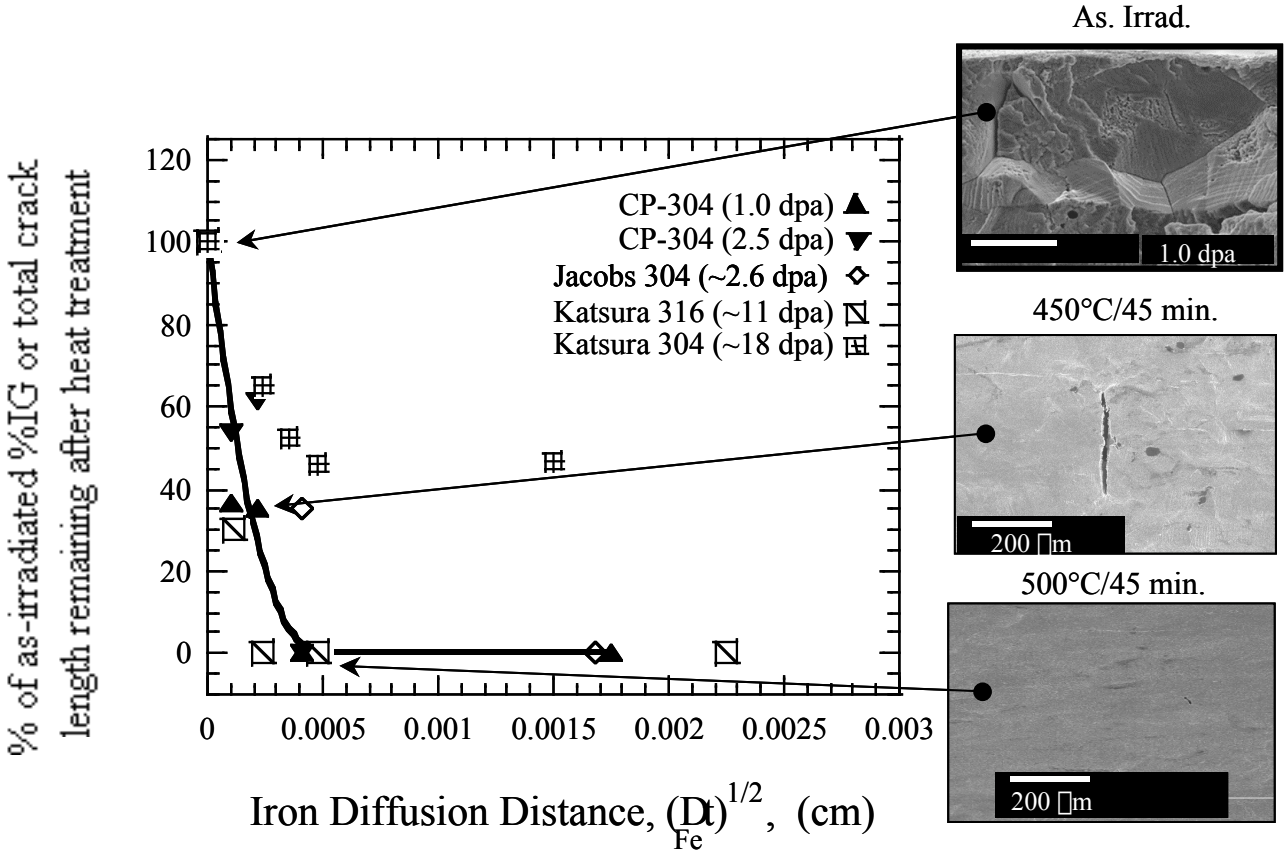

Figure 14. Comparison of measured total crack length or %IG remaining as a function and Fe-diffusion distance. Also, the irradiated surface of CP-304-2.5 dpa sample post-irradiation annealed at 450°C and 500°C for 45 min are shown. Samples strained at 3 x 10^{-7} s^{-1} in water at 288°C, 0.2 μS/cm, and 2 ppm O_2. A line has been added to the fracture surface of the sample annealed at 500°C for 45 min. to indicate the irradiated surface of the sample.

4.3 Discussion of Post-Irradiation Annealing Results

Simulations predicted that dislocation loops were removed preferentially over RIS. Comparison of the measured and simulated annealing confirmed the accuracy of the simulations for both segregation profiles and dislocation loops. The experimental separation of loops and RIS via post-irradiation annealing is confirmed in the following section. The effects of Cr, Si, and P segregation in IASCC are then examined by comparing the behavior of cracking and RIS during annealing. In a similar manner, the importance of dislocation loops and hardness in IASCC are determined.

4.3.1 Separation of RIS and Loops

The effects of post-irradiation annealing on microchemical changes were considerably different than those on microstructure and hardening. Very little change was observed in grain boundary composition or composition profiles in either alloy at most annealing conditions examined. Even under the most extreme conditions (600°C for 90 min.) radiation-induced segregation was largely unchanged. For all other conditions examined up to 600°C/90 min., measured microchemistry was virtually identical to the as-irradiated condition. Significant changes in loop population and hardness were observed following post-irradiation annealing, in contrast to the behavior observed for radiation-induced segregation. The data trends for the removal of RIS (Figure 8) and dislocation microstructure (Figure 11) are superimposed over the annealing of hardness shown in Figure 13. The removal of dislocation loops and hardness follow the same trend and both are clearly removed preferentially to RIS. Indeed, annealing at 600°C for 90 min. removed virtually all radiation-induced changes to yield stress. The preferential removal of dislocation loops and hardening is consistent with the annealing simulations. Further, RIS is not affected until 80% of the dislocation microstructure or hardening has been removed, which is consistent with the simulation results shown in Figure 6 and supports that the preferential removal of dislocation loops is partially due to competition for vacancies between the removal of RIS and loops.

In summary, measured results from both this study and other studies indicate that dislocation loops were removed preferentially over RIS. Comparison of the measured and

simulated annealing confirmed both the accuracy of the simulations and the preferential removal of the dislocation loop microstructure during annealing. Since microchemical changes were separated from microstructural changes and hardening, the cracking susceptibility following annealing was compared to the as-irradiated condition. Although, the cracking susceptibility was removed before RIS was truly isolated from the dislocation loops or hardening, careful comparison of the annealing behavior of both cracking and RIS may help to help assess the importance of RIS in IASCC. Direct comparisons of as-irradiated and annealed cracking susceptibility to as-irradiated and annealed dislocation loop microstructure and hardening provide further insight into the effect of each irradiation-induced change on IASCC.

4.3.2 RIS of Cr and Ni and IASCC

As shown in Figure 15 a.), the grain boundary Cr and Ni contents remain at the as-irradiated level over the range of annealing conditions (plotted as a function of Fe-diffusion distance) for both 1.0 and 2.5 dpa samples. However, IG cracking susceptibility clearly shows a very rapid decrease with increasing annealing time or temperature and is completely eliminated after annealing at 500°C for 45 min.

Given that the IG cracking susceptibility was removed before the grain boundary Cr content begins to change indicates that Cr depletion alone cannot be a primary contributor to IASCC. This result is consistent with the observed difference in cracking behavior of proton-irradiated CP-304 and the companion CP-316 alloy studied previously [29]. At all doses, the CP-316 exhibited more Cr depletion (in "w-shape" at 1.0 dpa or in "v-shape" at higher damage levels) than the CP-304 alloy, yet the CP-316 alloy did not crack at doses up to 5.0 dpa. Jacobs [46] also concluded in his study of neutron-irradiated 304 SS that the depletion of Cr does not appear to be a primary causative factor in IASCC."

Similarly, the grain boundary enrichment of Ni does not play an important role in the mitigation of IASCC as cracking was removed during annealing with no measurable change in Ni segregation. Grain boundary Ni content steadily increases with dose and is approximately twice the bulk level by 5.0 dpa. However, cracking susceptibility also increases steadily with increasing dose through 5.0 dpa, reinforcing that Ni enrichment cannot be a mitigating factor for IASCC.

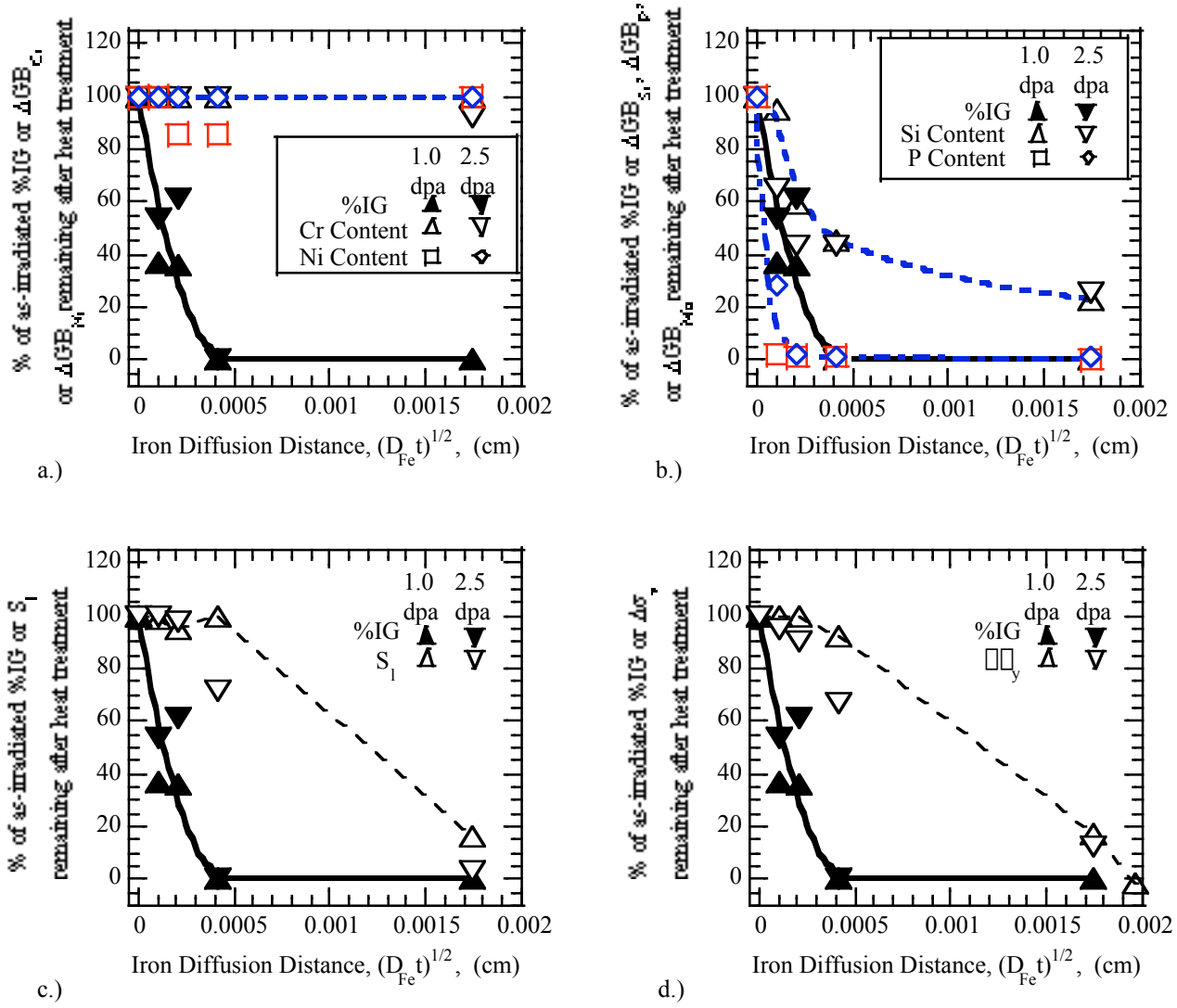

Figure 15. Comparison of annealing behavior of major alloying elements, a.), minor alloying elements, b.), dislocation loop line length, c.) and hardness, d.) with cracking susceptibility for CP-304 irradiated to 1.0 and 2.5 dpa.

4.3.3 RIS of Si and P and IASCC

Silicon and phosphorus enrichment and cracking susceptibility are compared in Figure 15 b.). During annealing, both Si and P enrichment are removed rapidly, at a rate similar to that of cracking susceptibility. The similarities in recovery rates of both Si and P enrichment to that of the cracking susceptibility potentially implicates both elements as contributors to IASCC.

However, substantial literature data suggest that Si plays a beneficial role, if any at all [45-50]. Chung [47] and Fukuya [48] both found that CP alloys with higher Si content were less susceptible to IG cracking than high purity alloys irradiated to the same conditions. Tsukada [49] reported that an alloy with high Si content failed at a higher strain than a high purity reference alloy with a comparable fraction of IG cracking. Only Jacobs et al. [50] reported any potential link between cracking and Si content. However, in a later study, Jacobs [46] reported grain boundary Si enrichment had little impact on IASCC. Finally, the work of Cookson [45] showed that increased Si content had a slightly beneficial effect on cracking of proton-irradiated HP-304 SS. Combined, the experimental evidence from other studies shows that the role of Si segregation in IASCC is minor.

The grain boundary P content of both 1.0 and 2.5 dpa samples, returned to the bulk content following even the shortest anneal (400°C for 45 min.), faster than the mitigation of cracking. While the percentage of IG cracking increases steadily with dose, the grain boundary P content increased dramatically between 0.3 and 1.0 dpa. Thereafter, the P content remained relatively unchanged until dropping back to the bulk level by 5.0 dpa (while cracking susceptibility continued to increase). The trends during annealing and dose dependence reveal that P enrichment during irradiation is the primary cause of IASCC, consistent with the work of Cookson [45], Fukuya et al. [48], Tsukada et al. [49], Chung et al. [15], and Jacobs [51] who all reported that P had either no effect or a slightly beneficial effect. While the results of this study indicate that the effects of minor alloying elements such as Si and P on IASCC to be minor, other minor alloying elements and impurities such as C, B, or N may be influential in IASCC.

4.3.4 Dislocation loops and IASCC

The total loop line length calculated from the dislocation loop microstructure is compared to the cracking susceptibility in Figure 15 c.). During annealing, the cracking susceptibility was mitigated before the total loop line length was significantly changed. No changes in loop density or diameter were measured following annealing at 400°C or 450°C for 45 min. The lack of change in loop line length after annealing at 500°C for 45 min. may be due to the inclusion of unfaulted loops in the density count.

With irradiation, the total dislocation line length associated with dislocation loops increased quickly with dose, reaching a saturation level between 1.0 and 3.0 dpa with little increase between 3.0 and 5.0 dpa. The cracking susceptibility, however, continued to increase considerably between 3.0 and 5.0 dpa. Further, dislocation densities and diameters measured in the proton-irradiated CP-316 SS alloy were similar to those measured in the CP-304 alloy [29]. Despite the similar loop populations, a distinct difference in cracking susceptibility exists. Therefore, the observed dislocation microstructure alone is not the primary mechanism for IASCC.

4.3.5 Hardening and IASCC

The impact of radiation-induced hardening is assessed in Figure 15 d.), which plots the change in yield stress and IG cracking susceptibility as a function of diffusion distance. During annealing of both 1.0 and 2.5 dpa specimens, the degree of hardening remains at the as-irradiated level for anneals at 400°C and 450°C. The hardening recovers slightly after annealing at 500°C for 45 min., while cracking has been completely removed, indicating that cracking susceptibility is not determined by hardness alone.

Like the dislocation loop microstructure, the change in yield stress increases steadily with increasing radiation dose up to 3.0 dpa. Between 3.0 and 5.0 dpa, there is little increase in yield stress change. Further, hardening of the proton-irradiated CP-316 alloy were similar to those measured in the CP-304 of this study in spite of the difference in cracking behavior [29]. Thus, radiation-hardening alone cannot explain the occurrence of IASCC in the alloys examined.

4.3.6 Other potential contributors to IASCC

The segregation of Cr, Ni, Si, and P were each found to be insufficient to cause IASCC alone. Further, the dislocation microstructure and radiation-induced hardening alone did not correlate with IASCC. All of these effects may contribute to IASCC, however, none seems to be sufficient to cause IASCC alone. Therefore, some other feature or radiation-induced change must be controlling the observed IASCC behavior. Possibilities include the segregation of other minor elements such as C, B, or N, which are not typically measured, unresolved small defect

clusters, or a combination of effects.

4.3.7 Other elements

The CP-304 alloy contains minor elements such as C, N, and B, which were not analyzed in this study. Quantitative analysis via STEM/EDS of B, C, or N is extremely difficult due to the low x-ray yields of these light elements. Further, significant peak overlap with lower energy peaks of major alloying elements such as Fe, Cr, and Ni makes even qualitative analysis difficult. The CP-304 and CP-316 studied by Was et al. [29] have similar levels of C (0.16 and 0.18 at%, respectively) and N (0.266 and 0.230 at%, respectively), making it difficult to explain the difference in cracking susceptibility between the two alloys on the basis of these elements alone.

Boron has been identified as potentially having beneficial effects on IASCC [52]. Chung et al. [15] reported that higher B concentration was beneficial in suppressing IASCC. In a study by Jenssen et al. [16], alloys with low boron content showed higher susceptibility to IASCC than those with higher bulk B levels. Boron was measured by Kenik et al. [53] using atom probe analysis in both the unirradiated CP-304 and CP-316 alloys studied by Was [29]. The grain boundary B content in the CP-316 SS was measured at 4.4 at%, considerably higher than the 1.4 at% content measured in the CP-304 SS, consistent with the observations of Chung [47] and Jenssen [16] and supporting the potentially beneficial role of B. However, analysis of the grain boundary B content must be performed on irradiated samples to confirm any potential role of B in suppressing IASCC. Other analytical techniques such as atom probe might be useful, however, techniques for creating atom-probe samples from proton-irradiated samples do not currently exist.

4.3.8 Combination of RIS and microstructure

RIS of any one element, the formation of dislocation loops or increases in hardness cannot alone account for the observed IASCC behavior. However, the presence of two or more effects at a critical level may be responsible, as suggested by Chung et al. [15]. The results of this study suggest that a combination of RIS, dislocation loops, and/or hardening controlling IASCC is unlikely. Considering that the cracking susceptibility was mitigated with even the shortest

annealing treatment, prior to Cr or Ni segregation, dislocation loops, and hardening being altered, no combination of the effects examined in this study can be solely responsible. However, changes in both the dislocation loop population and hardness might occur at the same time and offset each other, as discussed previously.

4.3.9 Small defect clusters

If none of the observed changes are responsible for the increase in cracking susceptibility with increasing dose, some other irradiation-induced change may be responsible. Fine scale radiation damage may be one of several possible contributors. During irradiation, interstitials or vacancies survive the cascade event, either as individual defects or as small clusters. The small clusters can take the form of vacancy or interstitial loops, stacking fault tetrahedra, di- or tri-vacancy clusters, interstitial clusters or defect-impurity clusters. During deformation of the sample, these small defects clusters will act to impede moving dislocations, similar to faulted dislocation loops. Unfortunately, small defect structures are typically not characterized due to the extreme difficulty in imaging this type of damage in TEM. Further, detailed and accurate analysis of small defect clusters is complicated as routine sample preparation of TEM disks typically involves the use of ion-milling to obtain an electron transparent region and can induce small defect damage in metal samples. [54]

During post-irradiation annealing, small defects can be removed quickly via annihilation due to their small size, or they can spontaneously dissociate, leaving individual interstitials or vacancies behind. [55] Dislocation loops may absorb free interstitials to slightly increase the mean radius or they may absorb vacancies and be removed, as depicted schematically in Fig. 16. Detailed analysis of the smallest defects in the post-irradiation annealed specimens (CP-304 at 1.0 dpa) was performed with dark-field analysis. The bright-field, dark-field and dislocation loop size distributions measured from the dark-field images are shown in Figure 10. Indeed, the dislocation loop size distributions illustrated in Figure 10 do show that the smallest dislocation loops were removed at the lowest annealing temperatures while the larger loops remained unaltered. The increase in hardness due to an increase in loop size is offset by the removal of the small defect clusters resulting in no observable change in loop density. Hence, the net effect is a change in defect morphology with no discernible change in dislocation loop density or yield strength calculated from measured hardness.

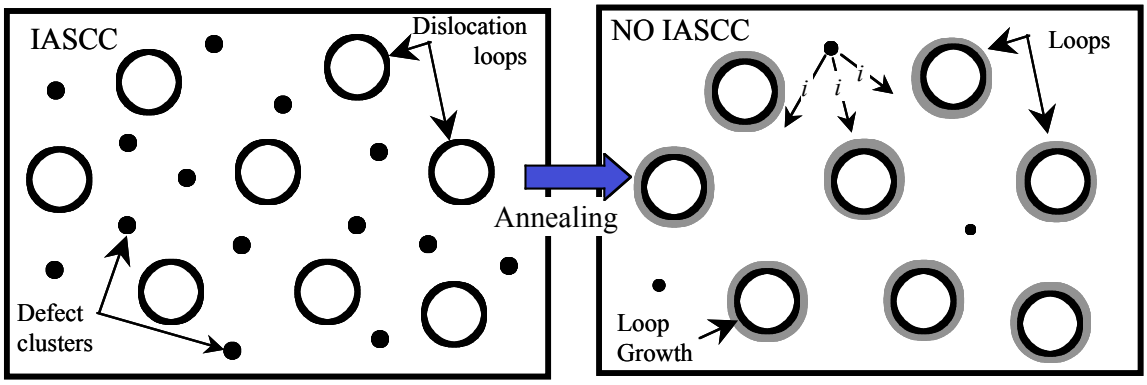

Figure 16. Schematic of annealing behavior of mixed population of black-dot damage and dislocations. During annealing, small defect clusters are removed or dissociate into individual interstitials which may then be absorbed by dislocation loops. This process results in a population of larger loops with no change in density.

Further information about the nature of the small defect populations may be gained by examining the post-irradiation annealing behavior of the samples irradiated at 360°C. In order to simulate the effects of post-irradiation annealing for a population of interstitial defects, the post-irradiation annealing model developed by Busby [56] was used. The model calculates the changes in loop radius and density as a function of time at any given temperature for a population of defects. The simulations were based on the methodology used by Burton [55] and further details are described by Busby. [56]

The annealing model has been applied to examine the annealing behavior of the smallest loops observed in the samples irradiated at 360°C and post-irradiation annealed. The loop density measured in each size up to 6 nm is plotted in Figure 17 for both the samples annealed at 450°C and 500°C. The simulated distributions for the same annealing conditions are also plotted in Figure 17 b.) for comparison. There is excellent agreement between the modeled and measured loop size distributions. The modeled and measured dislocation density (m^{-2}) for the smallest loops (less than 6 nm) is plotted in Figure 17 c. Again, there is excellent agreement between modeled and measured loop densities following annealing. This indicates that these small defects in the samples irradiated at 360°C are, indeed, small, faulted dislocation loops. This is in agreement with the recent results of Edwards et al. [57]

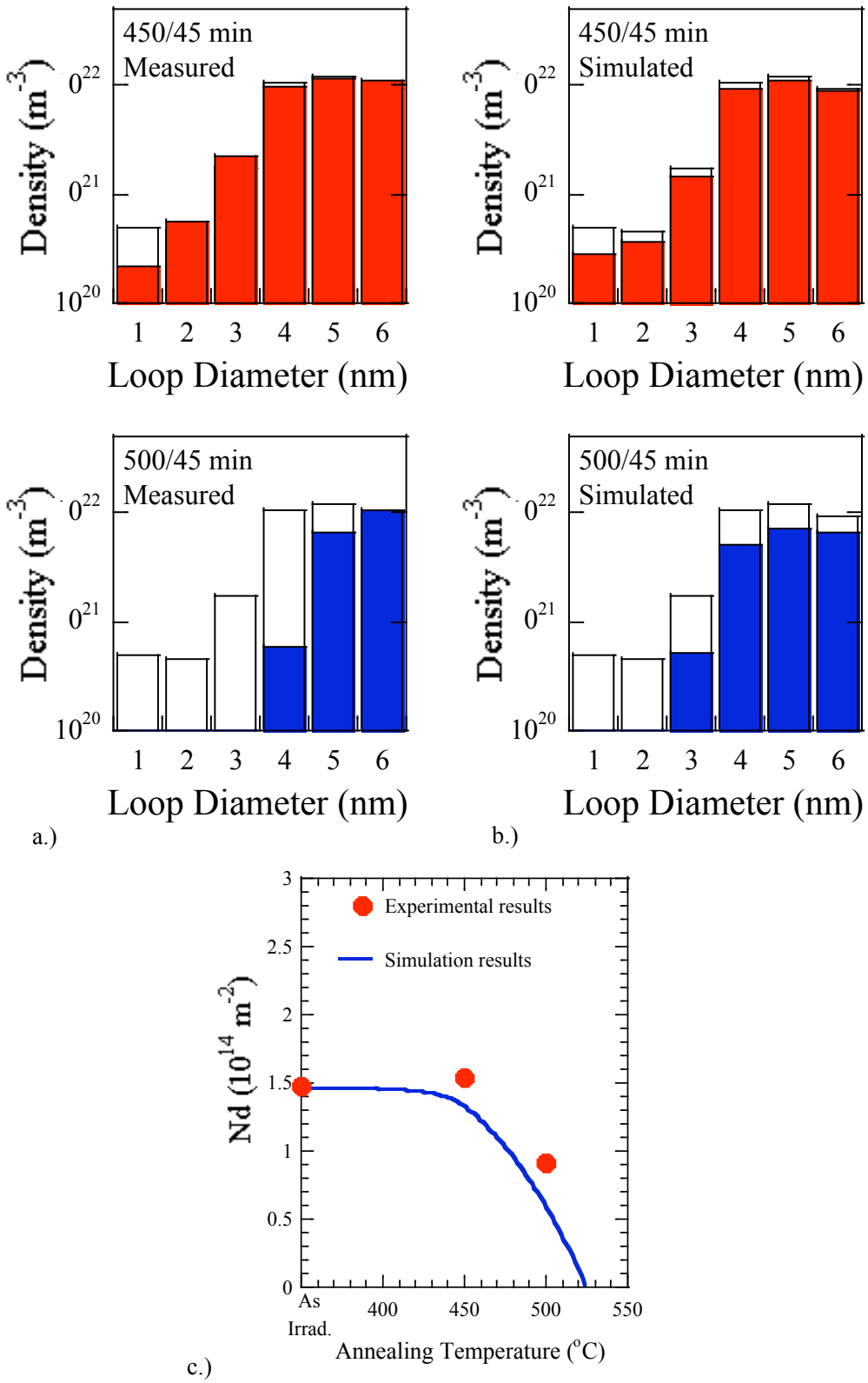

Figure 17. Comparison of measured and simulated annealing of small dislocation loop populations from proton irradiations to 1.0 dpa at 360°C (plotted as Nd in c.)).

4.3.10 Implications for IASCC

As noted earlier, the interaction between small loops and moving dislocations may result in dislocation channeling. In the channeling process, the initial, moving dislocations encounter dislocation loops, which act as barriers to the dislocations. To overcome these barriers, dislocations annihilate or combine with the defects on the slip plane and continue to glide. Subsequent dislocations will tend to glide along this same path, clearing out additional defects, resulting in a channel that is free of defects. The elimination of the irradiation induced defects along the primary slip planes results in localized deformation. These channels have been observed in both pure metals [58] and in austenitic stainless steels following irradiation with protons. [59] Channeling is more pronounced in alloys where the damage is in the form of a high density of small defects as opposed to a dislocation network.

As noted by Bruemmer et al, [59] localized deformation can be detrimental to IASCC by promoting dislocation pileups at grain boundaries. To accommodate local strain, a grain boundary may absorb dislocations, emit new dislocations, create deformation microtwins, or crack if no further strain can be accommodated. Further, dislocation channels may have a finite life before pile-ups occur closing the channel to further dislocation glide. As available channels for plasticity are eliminated, the grain boundary may not be able to accommodate further strain by emitting new dislocations or microtwins. This is consistent with recent results from Alexandreanu, [60] which examined IG cracking in Ni-base alloys. Alexandreanu found that boundaries that accommodate deformation by absorbing dislocations are also more susceptible to cracking.

Localized deformation has been observed in the post-irradiation annealed specimens of this study. Micrographs of the slip bands observed in the samples annealed at 450°C and 500°C for 45 minutes are compared in Figures 18 a and b. Slip bands were observed in both samples, although fewer bands were observed in the sample annealed at 500°C for 45 minutes, which failed with no evidence of IG cracking (25 slip band systems/mm2) while the sample annealed at 450°C for 45 minutes did have IG cracking and a higher density of bands ($65/mm^2$). The CP-304 sample irradiated to 0.3 dpa at 360°C also failed via ductile rupture, and the slip bands for this condition are shown in Figure 18c. The number of slip bands in the 0.3 dpa sample ($22/mm^2$) is comparable to those observed in the sample annealed for 45 minutes at 500°C. If fine-scale damage is a primary contributor to IASCC and removed rapidly during post-irradiation

annealing, a distinct difference in slip bands should be observed between annealed samples which exhibited cracking (1.0 dpa sample annealed at 450°C for 45 minutes), and those which failed via ductile rupture (1.0 dpa sample annealed at 500°C for 45 minutes). In the sample annealed at 450°C for 45 minutes, the higher density of slip bands in samples exhibiting cracking suggests that microstructural features such as fine scale clusters may be important in deformation, and hence, cracking susceptibility.

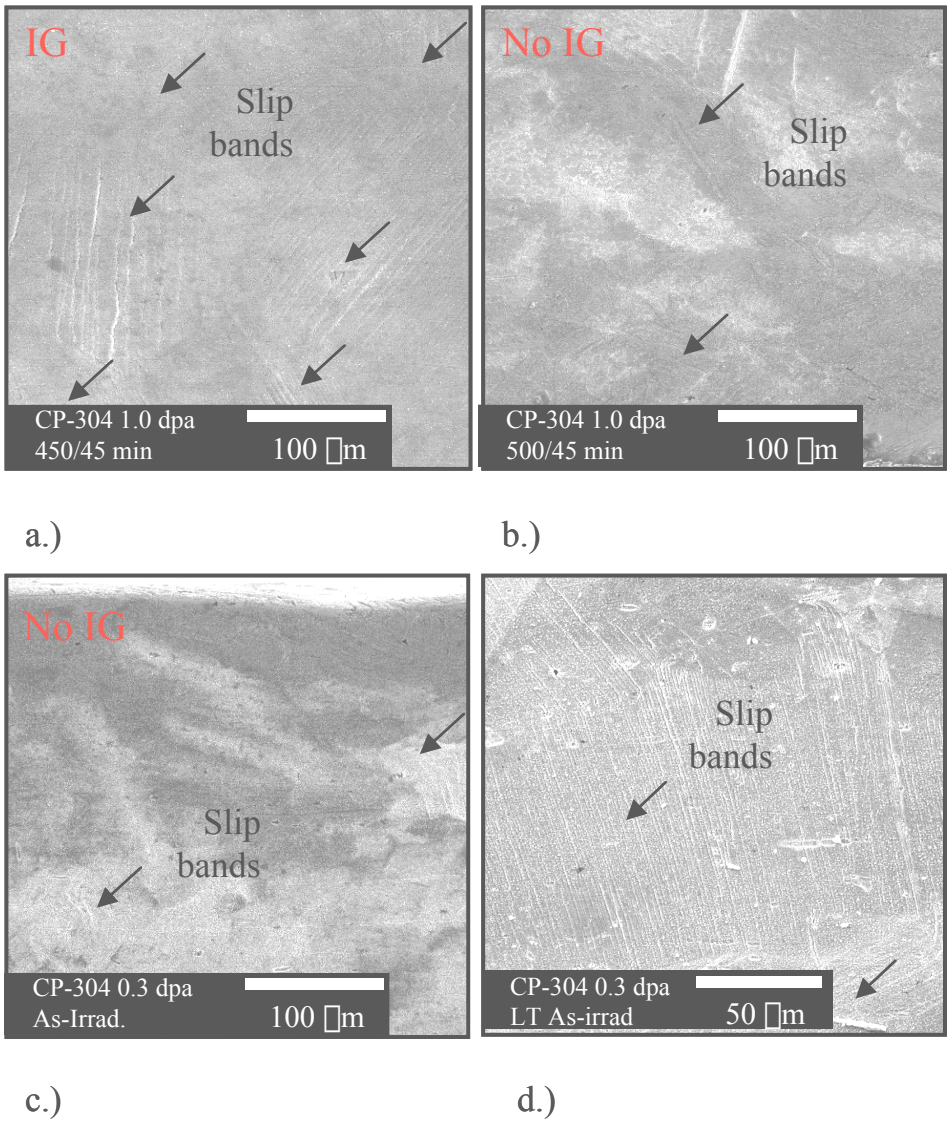

Figure 18. Comparison of slip bands in CP 304 SS irradiated to 1.0 dpa at 360°C and annealed at a.) 450°C/45 minutes (IG with 65 slip band systems/mm^2) or b.) 500°C/45 minutes (no IG and 25 slip band systems/mm^2). Also shown in c.) are the slip bands observed on a CP 304 SS sample irradiated to 0.3 dpa at 360°C (no IG with 22 slip band systems/mm^2) and d.) 0.3 dpa at < 75°C (no IG with 28 slip band systems/mm^2). Samples strained at 3.5 x 10^{-7} s^{-1} in water at 288°C, 0.2 □S/cm, and 2 ppm O_2.

Finally, note the mitigation of cracking during post-irradiation annealing shown in Figure 14 for this study is very similar to that of Jacobs and Katsura (with the exception of Katsura's 304 SS at a diffusion distance of 0.0016 cm). The similarity in cracking mitigation, despite the wide disparity in as-irradiated dose, indicates that cracking is controlled by a feature or condition, which has reached a critical level by 1.0 dpa (since cracking was observed at this dose). The fine defect damage reaches its saturation level very quickly during irradiation. [61] The rapid removal of a dense population of small obstacles impeding dislocation motion could result in a change in deformation mode and, hence, cracking behavior during annealing. This is consistent with the work of Bailat et al., [62] who reported a possible correlation between deformation mode and IASCC in neutron-irradiated stainless steels. Bailat et al. found localized deformation (channeling and microtwinning) in a susceptible 304 SS alloy using TEM analysis. A companion 316 alloy irradiated to the same conditions did not exhibit the same characteristics of localized deformation and was resistant to IASCC.

Low temperature irradiation is another means of examining fine scale radiation damage. Low temperature irradiations can create a relevant irradiation-induced microstructure, consisting primarily of a high density of small defect clusters, or black dot damage without the accompanying RIS. The following section presents results of the low temperature irradiations designed to isolate the irradiated microstructure.

4.4 Isolating the Dislocation Microstructure

Low-temperature irradiations were conducted to create a high density of small defect clusters. Two irradiation programs were completed, the first to a dose of 0.3 dpa at T<75°C, and the second to doses of 0.5 to 1.5 dpa in varying combinations of low (<75°C) and high (360°C) temperature irradiation designed to achieve a stable irradiated microstructure. The increase in hardness of samples irradiated to 0.3 dpa at T<75°C is about 75 kg/mm^2, which is higher than the value of 65 kg/mm^2 obtained after 1.0 dpa at 360°C. The high degree of hardening in the specimens irradiated to 0.3 dpa at T<75°C indicates that a very high density of defects has indeed been created. Subsequent annealing at temperatures between 350°C and 500°C resulted in annealing of the defects and a reduction in hardness, table 7 and Fig. 19. However, no visible defects have been observed in any of the as-irradiated or post-irradiation annealed specimens. TEM has the capability to resolve dislocation loops down to about 1.0 nm in diameter, and to

detect smaller loops. This indicates that the defects created during low temperature irradiation are less than 1 nm in diameter.

Table 7. Hardness of CP304 SS following irradiation and annealing.

Condition	ΔH_v (kg/mm^2)	Relative Hardness
Reference condition: 1.0 dpa@360°C	60	1.0
As-irrad. 0.3 dpa @ 50°C	85	1.42
As-irrad. + 3.8 hr @ 350°C	66	1.09
As-irrad. + 0.5 hr @ 400°C	35	0.59
As-irrad. + 0.5 hr @ 450°C	27	0.45
As-irrad. + 0.5 hr @ 500°C	23	0.36

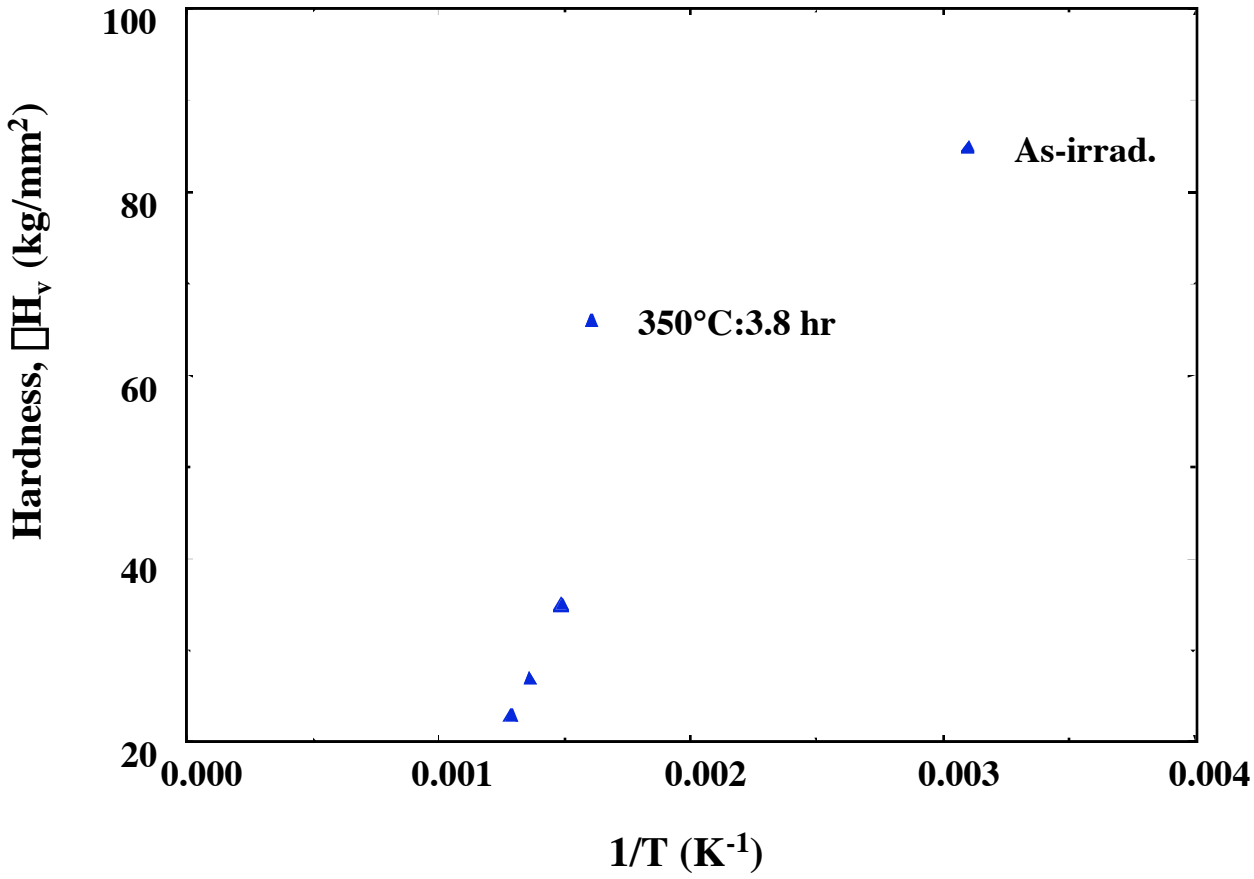

Figure 19. Change in hardness of CP304 SS following annealing of samples irradiated to 0.3 dpa at T<75°C.

Figure 20 confirms that following low temperature irradiation to 0.3 dpa, there is no evidence of RIS. As shown, chromium, nickel and iron contents are nearly flat across the grain boundary. Even silicon, which segregates strongly under irradiation, shows no sign of RIS, indicating that irradiation at low temperature was indeed successful in suppressing RIS.

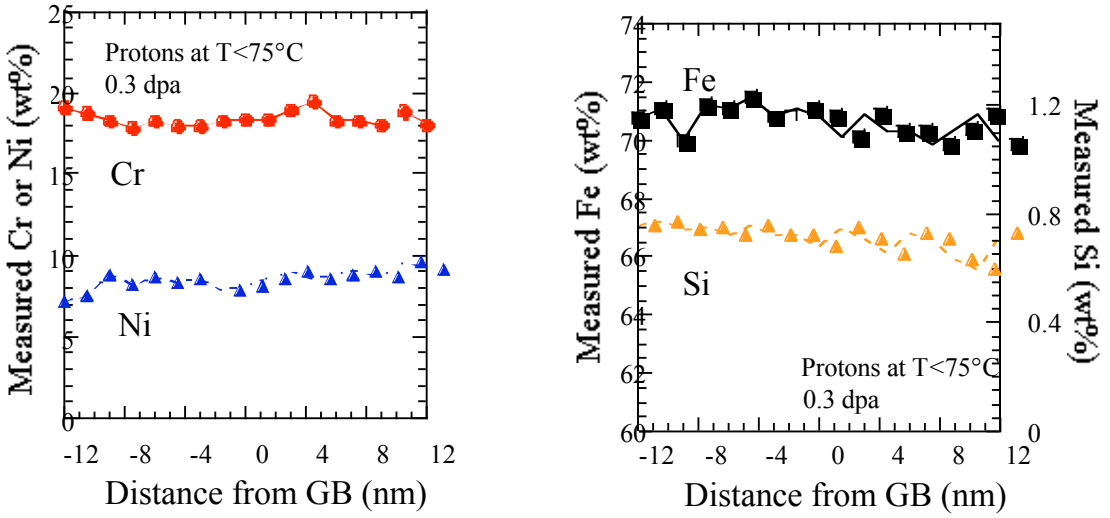

Figure 20. Composition profiles for Cr, Ni, Fe and Si across grain boundaries of CP304 SS following low temperature irradiation at T<75°C showing the lack of RIS.

A second series of irradiations was conducted to try to stabilize and grow the defect clusters using combinations of low and high temperature irradiations. Figure 21 shows the scheme for combinations of low and high temperature irradiations. Both TEM bars and SCC bars were irradiated to doses of 0.5 dpa on each step. Consequently, samples received total doses of between 1.0 and 1.5 dpa. Hardness results are given in table 8 and confirm that irradiation at low temperature or at high temperature followed by low temperature result in greater hardening than at high temperature or low temperature followed by high temperature. The results are quite consistent and indicate again that the density of very small defects following low temperature irradiation must be very high.

Stress corrosion cracking tests in normal water chemistry were conducted on the combination of low and high temperature irradiations shown in table 9. The stress-strain curves are given in Fig. 22. Note that with one exception, the samples all reached similar levels of stress and strain. Post-test inspection in the SEM revealed no IGSCC in these samples.

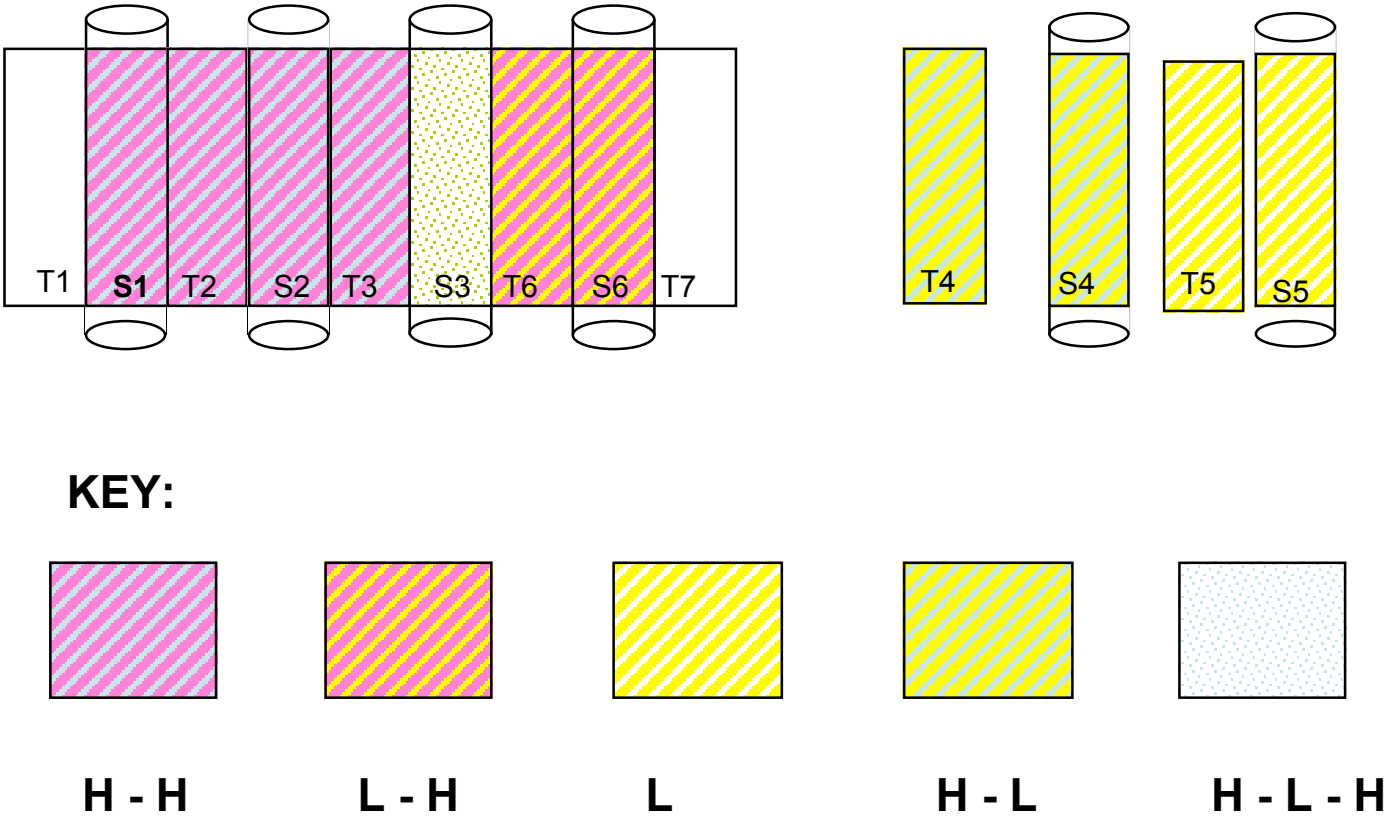

Figure 21. Scheme for achieving a stable irradiated microstructure by combining high temperature (T=360°C) and low temperature (T<75°C) irradiation in increments of 0.25 dpa.

Table 8. Hardness before and after various irradiations to 0.5 dpa at either T<75°C or at 360°C. All hardness units are in kg/mm^2.

Sample #	Unirradiated hardness	Hardness at 0.5 dpa@ 360°C	ΔH from previous condition	Hardness at 0.5 @ 75°C	ΔH from previous condition	Hardness at 0.5 dpa @ 360°C	ΔH from previous condition
T2	203	258	55	-	-	258	0
T3	206	261	55	-	-	258	-3
T4	207	256	49	313	57	-	-
T5	205	-	-	283	78	-	-
T6	205	-	-	298	93	248	-50

This is not surprising in retrospect as the low temperature irradiated microstructure is not stable at the SCC test temperatures. Figure 23 shows the decrease in hardness following an anneal for various times at temperatures at the SCC test temperature of 288°C. The softening in the CERT test is likely to be even more extensive than shown here as these tests ran for a duration of about 15 days.

Table 9. Results of constant extension rate test in 288°C BWR normal water chemistry.

Sample	Irradiation History	% Strain at failure	UTS(ksi)	# of cracks in irradiated region	Total Crack Length on irradiated Surface(_m)	Location of Failure	Fracture Mode	% IG	% TG	% Duc.
S2	1.0 dpa 360-360	36.2	63.6	1	1870 52	Irradiated Region	IG+TG +Ductile	2.0	38.8	59.7
S3	1.5 dpa 360-75-360	35.8	63.9	4	428 12	Threads	NA	NA	NA	NA
S4	1.0 dpa 360-75	31.6	63.0	1	1900 60	Irradiated Region	TG+ Ductile	0	18	82
S6	1.0 dpa 75-360	31.8	55.9	3	131 4	Unirr. Region	NA	NA	NA	NA
Ref.	1.0 dpa 360	23.6	64.9	1	1420 60	Irradiated Region	IG+TG +Ductile	2.2	61.7	36.1

While the current TEM analysis techniques have failed to reveal any information about the nature of these defects, some insight may be gained using the hardness results and simulations of post-irradiation annealing. Using the measured change in hardness for the as-irradiated specimen, the corresponding change in yield stress can be calculated using Eq. (1). An expected change in yield stress can also be calculated from irradiated microstructure using the dispersed barrier-hardening model [36]:

$$\Delta\sigma_y = \alpha M \mu b (Nd)^{1/2} \quad (7)$$

where a is the barrier strength (0.2 for small clusters [63], M is the Taylor factor (3.06), m is the shear modulus (76 GPa), b is the Burgers vector (0.255 nm), N is the defect density and d is the defect diameter. Using the calculated change in yield stress of 263 MPa, determined from the

hardness measurements, Nd can be determined as 5 x 10^{14} m^{-2}. If a mean cluster size of 0.5 nm is assumed (being approximately half of the smallest loop size measured in the samples irradiated at 360°C), the defect density is approximately 1 x 10^{24} m^{-3}. While this density is considerably higher than the loop density measured in the same alloy irradiated at 360°C, it is not an unreasonable density for small defect clusters created during low temperature irradiation. There is little data on microstructure development at low temperatures, although in a review paper, Zinkle [64] notes that the saturation density of small defect clusters may be greater than 10^{24} m^{-3}, and that this density is attained after doses of about 0.1 dpa. Further, the data from Higgy and Hammad [65] suggest that mechanical property measurements on 304 and 316 SS after neutron irradiation at <100°C suggest that defect cluster saturation occurs before 0.1 dpa, consistent with the results of this study.

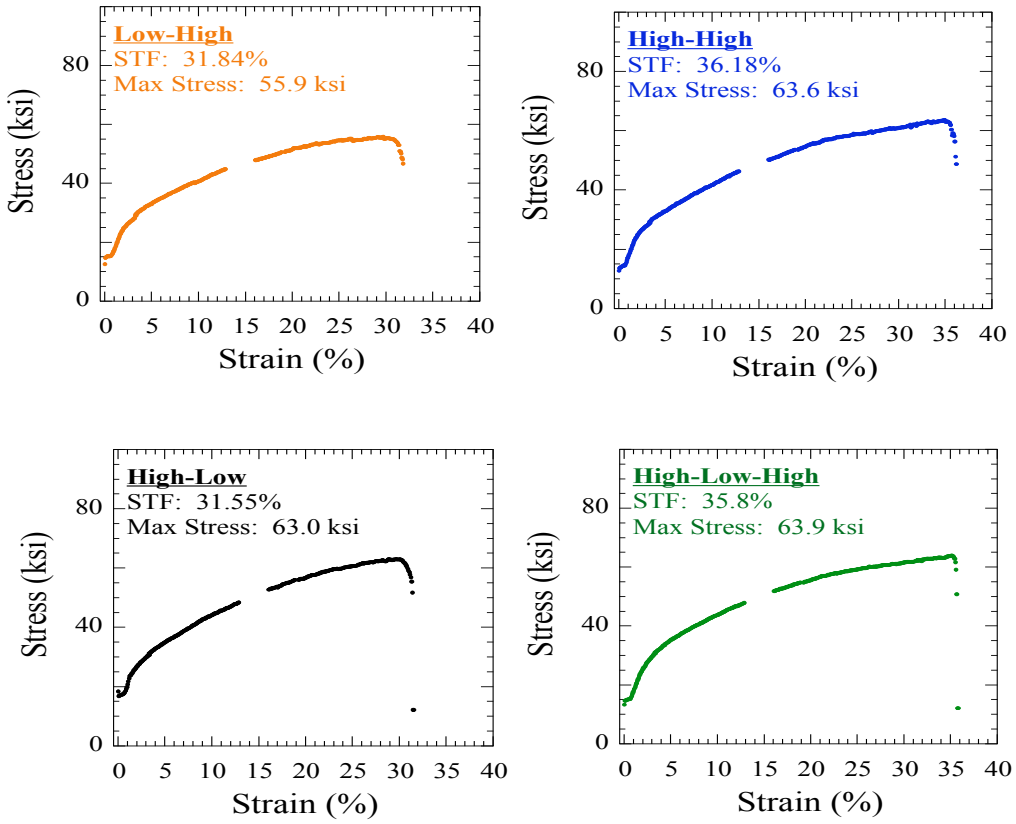

Figure 22. Stress-strain curves of CP304SS samples tested in normal water chemistry consisting of 288°C water containing 2 ppm O_2 and conductivity of 0.2 □S/cm. Samples were irradiated to the following conditions: a) 0.25 dpa @ T<75°C + 0.25 dpa @ 360°C, b) 0.25 dpa @ 360°C + 0.25 dpa @ 360°C, c) 0.25 dpa @ 360°C + 0.25 dpa @ T<75°C, and d) 0.25 dpa @ 360°C + 0.25 dpa @ T<75°C + 0.25 dpa @ 360°C.

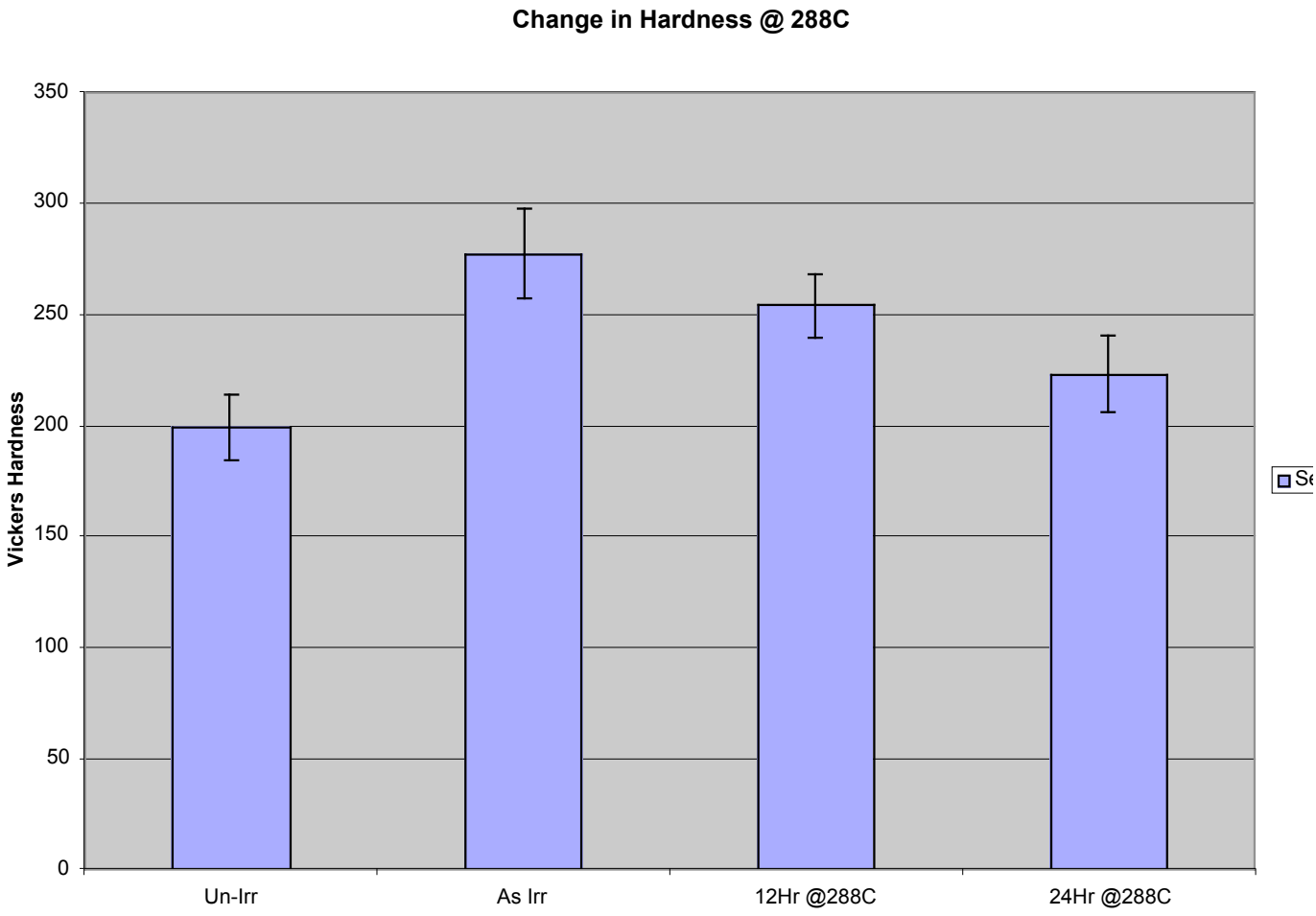

Figure 23. Change in hardness of CP304SS following irradiation to 0.3 dpa and annealing at 288°C for various times up to 24 hours.

The model developed by Busby has also been used to simulate the annealing of samples irradiated at low temperature. The as-irradiated defect density determined earlier was used as the initial condition in the simulations. A mean diameter of 0.5 nm, as discussed above, was assumed with the defect population being uniformly distributed between 0 to 1 nm. The experimental data is plotted along with simulation results in Figure 24. All results are plotted as Nd (calculated from hardness for the experimental results) as a function of annealing time. Clearly, the simulation at 350°C (solid line) predicts that the defect population is removed much slower than experimentally observed. Indeed, a temperature of 475°C is required for the simulations to match the experimental results. This discrepancy can be explained as follows.

First, the defect clusters in the simulations can only shrink by vacancy absorption, as there is no mechanism in the model for spontaneous dissolution. More significantly, the model developed by Busby only considers clusters that are interstitial in nature (as most dislocation loops are considered to be). Fine scale clusters are likely a mixed population of interstitial and vacancy type. Small vacancy clusters created under low temperature irradiation conditions are likely to dissociate rapidly following even low temperature annealing. Further, if vacancy and/or interstitial defect clusters spontaneously dissociate, this will provide additional vacancies and/or interstitials, which may be absorbed at other clusters. All these factors combined would result in accelerated annealing in the simulations, similar to what is experimentally observed.

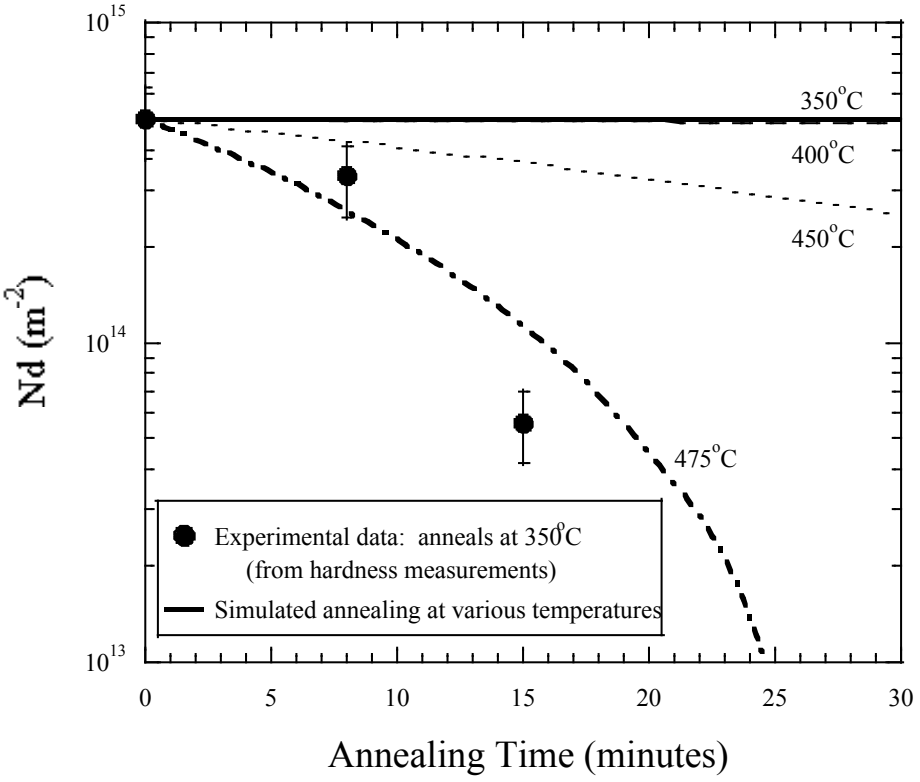

Figure 24. Comparison of annealing of samples irradiated at low temperatures with model simulations of annealing of small defect clusters.

Further simulations were performed using a model developed by Simonen. [66] The model developed by Simonen accounts for both interstitial and vacancy type loops or clusters. Clusters can absorb or emit vacancies or interstitials resulting in growth or reduction,

respectively, for a vacancy cluster (and vice-versa for an interstitial cluster). The simulation predictions for hardness after annealing are plotted in Fig. 25 as a function of adjusted time at temperature (a simple variable which combines accounts for changes in both annealing time and temperature). The hardness data from previous studies of post-irradiation annealing on proton-irradiated samples are also plotted for comparison. The model and measured results from higher temperature irradiations are in excellent agreement. The results from the low temperature irradiations and anneals are also plotted in Fig. 25. However, these measured recovery occurs much faster than that predicted by Simonen's model. The discrepancy between modeled and measured results indicates that the assumed ratio of vacancy to interstitial clusters does not represent the low temperature irradiations. In this simulation, 40% of the clusters were assumed to be vacancy-type. However, the rapid annealing of samples irradiated at low temperature indicate that this percentage is likely to be 50% or higher. Nevertheless, agreement between model and experiment is excellent.

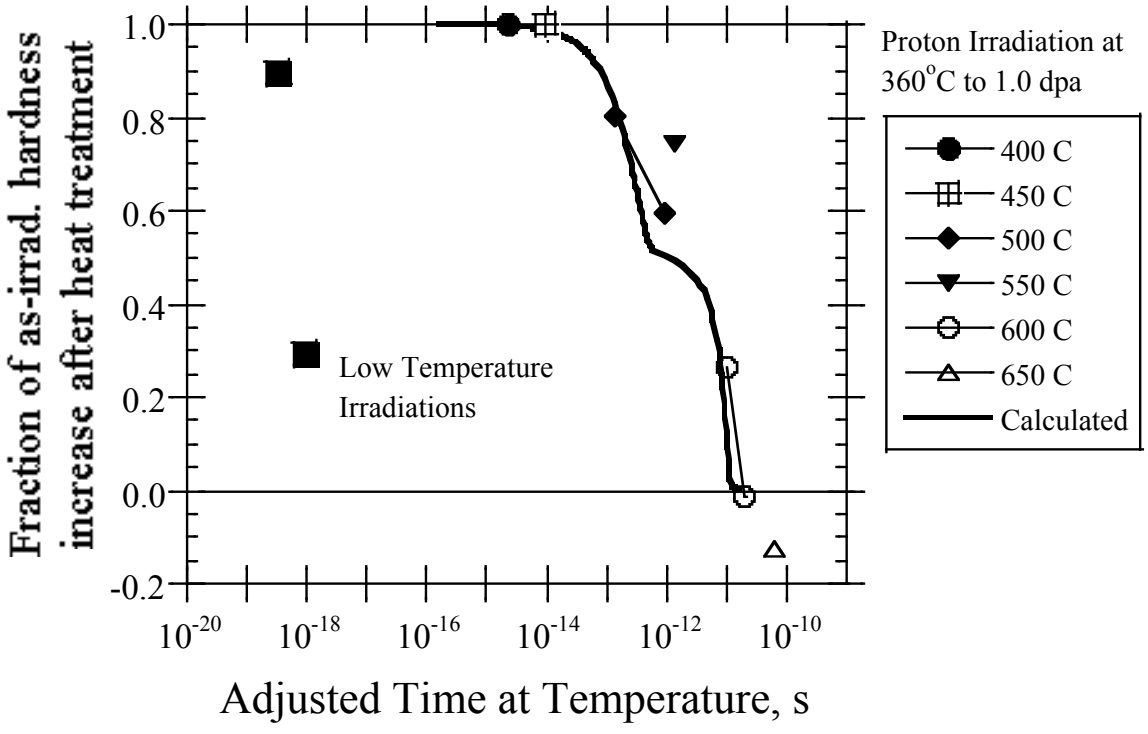

Figure 25. Comparison of annealing of samples irradiated at low temperatures with predictions from model developed by Simonen.

2.0 CONCLUSIONS

A radiation annealing model was developed that describes the elimination of dislocation loops by vacancy absorption. Results showed that there were indeed, time-temperature annealing combinations that leave the radiation induced segregation profile largely unaltered while the dislocation microstructure is significantly reduced. Proton irradiation of 304 stainless steel irradiated with 3.2 MeV protons to 1.0 or 2.5 dpa resulted in grain boundary depletion of chromium and enrichment of nickel and a radiation damaged microstructure. Post irradiation annealing at temperatures of 500 – 600°C for times of up to 45 min. removed the dislocation microstructure to a greater degree with increasing temperatures, or times at temperature, while leaving the radiation induced segregation profile relatively unaltered. Constant extension rate tensile (CERT) experiments in 288°C water containing 2 ppm O_2 and with a conductivity of 0.2 μS/cm and at a strain rate of 3×10^{-7} s^{-1} showed that the IASCC susceptibility, as measured by the crack length per unit strain, decreased with very short anneals and was almost completely removed by an anneal at 500°C for 45 min. This annealing treatment removed about 15% of the dislocation microstructure and the irradiation hardening, but did not affect the grain boundary chromium depletion or nickel segregation, nor did it affect the grain boundary content of other minor impurities. These results indicate that RIS is not the sole controlling feature of IASCC in irradiated stainless steels in normal water chemistry.

The isolation of the irradiated microstructure was approached using low temperature irradiation or combinations of low and high temperature irradiations to achieve a stable, irradiated microstructure without RIS. Experiments were successful in achieving a high degree of irradiation hardening without any evidence of RIS of either major or minor elements. The low temperature irradiations to doses up to 0.3 dpa at T<75°C were also very successful in producing hardening to levels considerably above that for irradiations conducted under nominal conditions of 1 dpa at 360°C. However, the microstructure consisted of an extremely fine dispersion of defect clusters of sizes that are not resolvable by either transmission electron microscopy (TEM) or small angle x-ray scattering (SAXS). The microstructure was not stable at the 288°C IASCC test temperature and resulted in rapid reduction of hardening and presumably, annealing of the defect clusters at this temperature as well. Nevertheless, the annealing studies showed that

treatments that resulted in significant decreases in the hardening produced small changes in the dislocation microstructure that were confined to the elimination of the finest of loops (~1 nm). These results substantiate the importance of the very fine defect microstructure in the IASCC process.

The results of this program provide the first definitive evidence that RIS is not the sole controlling factor in the irradiation assisted stress corrosion cracking of austenitic stainless steels in normal water chemistry. Earlier research has suggested that RIS may not play the dominant role it has recently been afforded, but the results of this program are the first to definitively establish this role. The program has also shown that the fine defect structure is implicated in the IASCC process and likely plays a role in the observed cracking of core components. The results of this project provide the basis and the motivation for further investigation into the mechanism of IASCC in which fine defect clusters may play a crucial, if not a defining role.

6.0 REFERENCES

1. P.L. Andresen, F.P. Ford, S.M. Murphy, J.M. Perks, *Proc. Fourth Int'l Symp. on Environmental Degradation of Materials in Nuclear Power Systems - Water Reactors*, NACE, 1990, pp. 1-83 to 1-121.
2. A. J. Jacobs, Letter Report and Literature Search, GE Nuclear Energy, San Jose, CA, May, 1979.
3. F. Garzrolli, H. Rubel and E. Steinberg, in *Proc. First Int'l Symp. on Environmental Degradation of Materials in Nuclear Power Systems - Water Reactors*, NACE, Houston, 1984, p. 1.
4. H. Hanninen and I. Aho-Mantila, in *Proc. Third Int'l Symp on Environmental Degradation of Materials in Nuclear Power Systems - Water Reactors*, AIME, Warrendale, 1988, p. 77.
5. V. Pasupathi and R. W. Klingensmith, "Investigation of Stress Corrosion Cracking in Clad Fuel Elements and Fuel Performance in the Connecticut Yankee Reactor," NP-2119, Electric Power Research Institute, 1981.
6. G.M. Gordon and K.S. Brown, *Proc. Fourth Int'l Symp on Environmental Degradation of Materials in Nuclear Power Systems - Water Reactors*, NACE, 1990, p.14-46.
7. K.S. Brown and G.M. Gordon, *Proc. Third Int'l Symp on Environmental Degradation of Materials in Nuclear Power Systems - Water Reactors*, AIME, 1987, pp. 243-248.
8. C. F. Cheng, *Corrosion* 20 (1964) 341.
9. P.M. Scott, W. Foot, L.A. Goldsmith, S. Dumbill, T.M. Williams, J.M. Perks, C.A. English and W.G. Burns, in NEA/UNIPEDE Specialists Mtg on Life Limiting and Regulatory Aspects of Core Internals and Pressure Vessels, Stockholm, Oct 14-16, 1987.
10. Garzarolli, D. Alter and P. Dewes, *Proc. Second Int'l Symp on Environmental Degradation of Materials in Nuclear Power Systems - Water Reactors*, 1986, ANS, p. 131.
11. P. Scott, *J. Nucl. Mater*. 211 (1994) 101.
12. S. Bruemmer, ed., Research Assistance Task Force on Radiation Materials Science, Palo Alto, Ca, March, 1998.
13. S. M. Bruemmer and G. S. Was, *J. Nucl. Mater.* 216 (1994) 326-347.
14. S. M. Bruemmer, in *Grain Boundary Chemistry and Intergranular Fracture*, eds. G. S. Was and S. M. Bruemmer, Trans Tech Publications, Switzerland, 1989, p. 309.
15. H. M. Chung, W. Ruther, J. Sanecki, A. Hins, N. Zaluzec and T. Kassner, *J. Nucl. Mater*. 239 (1996) 61.
16. A. Jenssen, and L. G. Ljungberg, in *Proc. Seventh Int'l Symp on Environmental Degradation of Materials in Nuclear Power Systems - Water Reactors*, NACE, Houston, 1996, p. 1043.
17. G. S. Was and T. Allen, JNM 205 (1993) 332.
18. D. L. Damcott, G. S. Was and S. M. Bruemmer, *Proc. Materials Research Society*, Vol. 373, Materials Research Society, Pittsburgh, 1995, p. 131.
19. R. D. Carter, D. L. Damcott, M. Atzmon, G. S. Was and E. L. Kenik, *J. Nucl. Mater.* 205 (1993) 361.
20. R. D. Carter, M. Atzmon, G. S. Was and S. M. Bruemmer, *Proc. Materials Research Society*, Vol. 373, Materials Research Society, Pittsburgh, 1995 p. 171.
21. T. Allen, G. S. Was and E. Kenik, *J. Nucl. Mater.,* 244 (1997) 278.
22. D. Damcott, D. Carter, J. Cookson, J. Martin, M. Atzmon and G. S. Was, *Rad. Eff. Def. Sol.* 118 (1991) 383.

23. J. M. Cookson, R. D. Carter, D. L. Damcott, M. Atzmon and G. S. Was, *J. Nucl. Mater.* 202 (1993) 104.
24. J. L. Hertzberg and G. S. Was, *Metall. Trans. A*, in press.
25. J. L. Hertzberg, K. Lian and G. S. Was, *Proc. Eighth Int'l Symp on Environmental Degradation of Materials in Nuclear Power Systems - Water Reactors*, American Nuclear Society, LaGrange Park, 1997, p. 257.
26. G. S. Was, in Critical Issue Reviews for the Understanding and Evaluation of Irradiation-Assisted Stress Corrosion Cracking, Electric Power Research Institute, Palo Alto, EPRI TR-107159, 1996, p. 6-1.
27. Todd Allen, Ph.D. thesis, University of Michigan, 1996.
28. A. Jenssen, and L. G. Ljungberg, Proc. Seventh Int'l Symp. on Environmental Degradation of Materials in Nuclear Power Systems - Water Reactors, NACE International, Houston, TX, 1995, p. 1043.
29. G. S. Was, J. T. Busby, J. Gan, E. A., Kenik, A. Jenssen, S. M. Bruemmer,P. M. Scott, and P. L. Andresen, *J. Nucl. Mater*., 300, (2002) 198-216.
30. J. T. Busby, Ph.D. Thesis, University of Michigan, 2001.
31. T. R. Allen, D. L. Damcott, G. S. Was, and E. A. Kenik, Proceedings of the 7th Env. Deg., NACE International, Houston, TX, 1995, 997
32. J. T. Busby, and G. S. Was, submitted to Met Trans A. 2003
33. G.S. Was, J. T. Busby, J. Gan, E. A. Kenik, A. Jenssen, S. M. Bruemmer, P. M. Scott, P. L. Andresen, accepted by J. Nucl. Mater.
34. P. L. Andresen, "Irradiation-Assisted Stress-Corrosion Cracking," in Stress–Corrosion Cracking, Materials Performance and Evaluation, Russell H. Jones, Ed., ASM International, Materials Park, OH, 1992, p. 181.
35. B. Burton, Mat. Sci. and Tech., Vol 8 (1992) p. 602.
36. A. Seeger, Proc. 2nd UN Int. Conf. On Peaceful Uses of Atomic Energy, Geneva, Sept., 1958, Vol. 6, p. 250.
37. A. Jacobs, Proceedings of the 7th Env. Deg, NACE International, Houston, TX, 1995, 1021.
38. S. Katsura, et al. Corrosion 98 Conference, NACE, paper 132.
39. S.M. Bruemmer, Private communication.
40. J.T. Busby, G.S. Was, and E.A. Kenik, Mat. Res. Soc. Symp. Proc. Vol. 540, 1998 MRS Fall Meeting, p. 451.
41. P. R. Okamoto and L. E. Rehn, J. Nucl. Mater. 83 (1979) p 2
42. H. Ullmain (Ed.), Atomic Defects in Metals, Landolt-Bornstein, New Series, Group 3, Vol. 25 (Springer-Verlag, City, 1991).
43. E. Simonen, D.J. Edwards, and S.M Bruemmer, to be published in Proceedings of Fall 2000 MRS Meeting, Boston, MA, 2000.
44. D. R. Olander, "Fundamental Aspects of Nuclear Reactor Fuel Elements", Published by Technical Information Center, Energy Research and Development Administration. 1976.
45. J. Cookson, Ph.D. Thesis, University of Michigan (1996).
46. A.J. Jacobs, 16th Int. Symp. On Radiation on Materials, ASTM-STP 1175, eds. A.S. Kumar, D.S. Gelles, R.K. Nanstad, and E.A. Little (ASTM, Philadelphia, 1993) p. 902.
47. H.M. Chung, W.E. Ruther, J.E. Sanecki, and T.F. Kassner, Proc. Fifth Int. Symp. On Env. Deg. Of Materials in Nuclear Power Systems-Water Reactors, D. Cubicciotti (Ed.), Monterey CA, ANS (1992) p. 795.
48. K. Fukuya, K. Nakata, A. Horie. Proc. Fifth Int. Symp. On Env. Deg. Of Materials in Nuclear Power Systems-Water Reactors, D. Cubicciotti (Ed.), Monterey CA, ANS (1992) p. 814.

49. T. Tsukada, Y. Miwa, and J. Nakajima, Proc. Seventh Int. Symp. On Env. Deg. Of Materials in Nuclear Power Systems-Water Reactors, R.E. Gold and E.P Simonen (Ed.), Breckenridge, CO, (199) p. 1009-1020.
50. Jacobs, C.M. Sheperd, G.E.C. Bell, and C.P. Wozaldo, Proc. Fifth Int. Symp. On Env. Deg. Of Materials in Nuclear Power Systems-Water Reactors, D. Cubicciotti (Ed.), Monterey CA,
52. P. L. Andresen, F. P. Ford, S. M. Murphy, and J. M. Perks, Proc. 4th Int. Symp. On Environmental Degradation of Materials in Nuclear Power Systems – Water Reactors, Jekyll Island, GA, Aug. 1989 (NACE, Houston, 1990), p. 1.
53. E. A. Kenik, J.T. Busby, M.K. Miller, A.M. Thuvander, and G.S. Was, Mat. Res. Soc. Symp. Proc. Vol. 540, 1998 MRS Fall Meeting, p. 445.
54. D. J. Barber, Ultramicroscopy, 52 (1993) p. 101-125.
55. B. Burton, *Materials Science and Technology*, Vol. 8, 1992 pp. 602.
56. J. T., Busby, G. S. Was, and E. A Kenik, *J. Nucl. Mater.*, Vol. 302, 2002, pp. 20-40.
57. D. J. Edwards, E. P. Simonen, and S. M. Bruemmer, J. Nucl. Mater., 317 (2003), p. 13-31.
58. P. J. Maziasz, and C. J. McHargue, *International Metal Review*., Vol. 32, 1987, pp. 190.
59. S. M. Bruemmer, J. I. Cole, J. L. Brimhall, R. D. Carter, and G. S. Was, *Proceedings of the 6th International Symposium On Environmental Degradation of Materials in Nuclear Power Systems – Water Reactors*, San Diego, CA, Aug, 1993, (TMS, 1993), pp. 537.
60. B. Alexandreanu, Ph.D. Thesis; University of Michigan, 2002.
61. S. J. Zinkle, P. J. Maziasz. and R. E. Stoller, *J. Nucl. Mater.*, Vol. 206, 1993, pp. 266-286.
62. C. Bailat, A. Almazouzi, M. Baluc, R. Schaublin, F. Groschel, and M. Victoria, *J. Nucl. Mater.*, Vol. 283-287, 2000, pp. 446-450.
63. G. E, Lucas, J. Nucl. Mater. 206 (1993) 287-305.
64. S. J. Zinkle, P. J. Maziasz, and R. E. Stoller, *J. Nucl. Mater.*, 206 (1993) 266-286.
65. H.R. Higgy and F.H. Hammad, J. Nucl. Mater. 55 (1975) 177-186.
66. E.P. Simonen, D.J. Edwards, B.W. Arey, S.M. Bruemmer, J.T Busby, and G.S. Was, To be published in the Phil. Mag. A., 2003.

7.0 PUBLICATIONS

J. T. Busby, M. M. Sowa, G. S. Was and E. P. Simonen, "Post-irradiation Annealing of Small Defect Clusters," submitted to Phil. Mag. A.

E. P. Simonen, D. J. Edwards, B. W. Airey, S. M. Bruemmer, J. T. Busby and G. S. Was, "Annealing Stages in Neutron-Irradiated Austenitic Stainless Steels," submitted to Phil. Mag. A.

G. S. Was, J. Busby, M. Sowa, M. Hash and R. Dropek, "Role of Irradiated Microstructure and Microchemistry in Irradiation Assisted Stress Corrosion Cracking," submitted to Phil. Mag. A.

G. S. Was and J. T. Busby, "Recent Developments in Irradiation Assisted Stress Corrosion Cracking," 10th Int'l Conf. Environmental Degradation of Materials in Nuclear Power Systems – Water Reactors, American Nuclear Society, LaGrange Park, IL, invited.

J. T. Busby, G. S. Was and E. A. Kenik, "Role of Radiation-Induced Segregation in IASCC of Austenitic Stainless Steels," J. Nucl. Mater., 302 (2002) 20-40.

G. S. Was, J. T. Busby, T. Allen, E. A. Kenik, A. Jenssen, S. M. Bruemmer, J. Gan, A. D. Edwards, P. Scott and P. L. Andresen, "Emulation of Neutron Irradiation Effects with Protons: Validation of Principle," J. Nucl. Mater., 300 (2002) 198-216.

J. T. Busby, M. M. Sowa and G. S. Was, "The Role of Fine Defect Clusters in Irradiation-Assisted Stress Corrosion Cracking of Proton-Irradiated 304 Stainless Steel," Effects of Radiation on Materials: 21st International Symposium, ASTM STP, M. L. Grossbeck, T. R. Allen, R. G. Lott and A. S. Kumar, Eds., American Society for Testing and Materials, West Conshohocken, PA, 2002.

J. T. Busby, G. S. Was and E. A. Kenik, "Isolation of the Role of Radiation-Induced Segregation in Irradiation Assisted Stress Corrosion Cracking of Proton-Irradiated Austenitic Stainless Steels," 10th Int'l Conf. Environmental Degradation of Materials in Nuclear Power Systems – Water Reactors, NACE International, Houston, TX, 2002.

J. T. Busby, J. Gan, M. Daniels, G. S. Was, S. M. Bruemmer, D. J. Edwards and E. A. Kenik, "Microchemistry and Microstructure Evolution in Proton-Irradiated Austenitic Stainless Steels," Proc. 9th International Conference on Environmental Degradation of Materials in Nuclear Power Systems - Water Reactors, Minerals, Metals and Materials Society, Warrendale, PA, 1999, pp. 1089-1098.

8.0 STUDENTS

A total of three students supported on this program received graduate degrees from the Department of Nuclear Engineering, University of Michigan.

Jeremy Busby received his PhD thesis on "Role of Radiation Induced Segregation in Irradiation Assisted Stress Corrosion Cracking," in December, 2000.

Ben Grambau received his MS degree in December, 2001.

Shawn Bilek received her MS degree in August, 2001.